Article

Calcium-permeable AMPA receptors govern PV neuron feature selectivity

Ingie Hong[1,2,25 ✉], Juhyun Kim[1,3,4,25], Thomas Hainmueller[5,21,25], Dong Won Kim[1,22,23], Joram Keijser[6,7], Richard C. Johnson[1,2], Soo Hyun Park[8,9], Nathachit Limjunyawong[1,24], Zhuonan Yang[1,2], David Cheon[1,2], Taeyoung Hwang[1,10,11], Amit Agarwal[1,12,13], Thibault Cholvin[5], Fenna M. Krienen[14], Steven A. McCarroll[15], Xinzhong Dong[1,16], David A. Leopold[8], Seth Blackshaw[1,2,17,18], Henning Sprekeler[6,19,20], Dwight E. Bergles[1,2], Marlene Bartos[5], Solange P. Brown[1,2] & Richard L. Huganir[1,2 ✉]

The brain helps us survive by forming internal representations of the external world[1,2]. Excitatory cortical neurons are often precisely tuned to specific external stimuli[3,4]. However, inhibitory neurons, such as parvalbumin-positive (PV) interneurons, are generally less selective[5]. PV interneurons differ from excitatory neurons in their neurotransmitter receptor subtypes, including AMPA (α-amino-3-hydroxy-5-methyl-4-isoxazole propionic acid) receptors (AMPARs)[6,7]. Excitatory neurons express calcium-impermeable AMPARs that contain the GluA2 subunit (encoded by *GRIA2*), whereas PV interneurons express receptors that lack the GluA2 subunit and are calcium-permeable (CP-AMPARs). Here we demonstrate a causal relationship between CP-AMPAR expression and the low feature selectivity of PV interneurons. We find low expression stoichiometry of *GRIA2* mRNA relative to other subunits in PV interneurons that is conserved across ferrets, rodents, marmosets and humans, and causes abundant CP-AMPAR expression. Replacing CP-AMPARs in PV interneurons with calcium-impermeable AMPARs increased their orientation selectivity in the visual cortex. Manipulations to induce sparse CP-AMPAR expression demonstrated that this increase was cell-autonomous and could occur with changes beyond development. Notably, excitatory–PV interneuron connectivity rates and unitary synaptic strength were unaltered by CP-AMPAR removal, which suggested that the selectivity of PV interneurons can be altered without markedly changing connectivity. In *Gria2*-knockout mice, in which all AMPARs are calcium-permeable, excitatory neurons showed significantly degraded orientation selectivity, which suggested that CP-AMPARs are sufficient to drive lower selectivity regardless of cell type. Moreover, hippocampal PV interneurons, which usually exhibit low spatial tuning, became more spatially selective after removing CP-AMPARs, which indicated that CP-AMPARs suppress the feature selectivity of PV interneurons independent of modality. These results reveal a new role of CP-AMPARs in maintaining low-selectivity sensory representation in PV interneurons and implicate a conserved molecular mechanism that distinguishes this cell type in the neocortex.

Genes dictate the response of a neuron to synaptic input and thereby program its biophysical computations[6,8]. For instance, neurotransmitter receptor profiles can determine the influx of Ca^{2+} to dendrites, which triggers neuronal changes that enable information storage[2,9,10]. Notably, gene expression varies widely across neuron types, which results in specialized roles within a given network and distinct responses to the same sensory input[11,12]. A key gene expression difference among the cardinal neuron types lies in their synaptic receptor composition[13,14]. Despite significant advances in understanding the role of synaptic protein genes, how these genes affect computations in the native brain is underexplored.

Neurons in the neocortex compute and represent features of the outside world through sparse, decorrelated activity[1]. This capability is particularly well characterized in the hippocampus, where place cells fire strongly to specific locations[3], and in the primary visual cortex (V1), where neurons are highly tuned to oriented edges or movement directions in the visual receptive field[4]. In the visual cortex, the response selectivity of a neuron for orientation, spatial frequency, colour or speed is conferred through organized synaptic inputs that arise from thalamocortical neurons and excitatory and inhibitory neurons from within the cortex[4,15]. However, the genes, receptors and plasticity

programs that give rise to this finely tuned circuit organization are largely unknown. A crucial clue to this question arises from the natural diversity of feature tuning expressed by different cell types[16]. Excitatory glutamatergic neurons display high orientation and direction selectivity, whereas PV GABAergic interneurons show low orientation selectivity[17–21] (but see ref. 22). This distinction seems consistent across various modalities, with PV neurons typically displaying less selectivity. For instance, in the hippocampus, PV cells show much lower spatial selectivity than adjacent excitatory place cells[5].

PV basket cells are highly adapted to fast spiking and provide strong and rapid feedback inhibition to nearby neurons[5]. They possess a distinct glutamate receptor profile, with small NMDA receptor (NMDAR) currents but large CP-AMPAR currents[7,23,24]. AMPARs are tetrameric glutamate receptors that mediate the majority of fast excitatory synaptic transmission in the brain. CP-AMPARs lack the voltage-dependent block of NMDARs by Mg^{2+}, which allows them to induce distinct Ca^{2+} dynamics and forms of plasticity at synapses[25,26]. This characteristic suggests that CP-AMPARs in PV neurons have the potential to continually shape and adjust the relative strengths of inputs that carry diverse types of information in a manner distinct from nearby excitatory neurons. Here we explore the consequences of high CP-AMPAR levels and reveal that they play an important part in maintaining the low orientation selectivity of PV interneurons.

Conserved AMPAR subunit mRNA stoichiometry

The calcium permeability of an AMPAR arises from two distinct routes, both involving GluA2: the lack of a GluA2 subunit (GluA2-lacking AMPAR) or the lack of RNA editing in the *Gria2* site that encodes a crucial pore amino acid of GluA2 (unedited GluA2)[23]. The lack of GluA2 in turn could be due to transcriptional or translational regulation. We analysed SmartSeq-based high-coverage single-cell RNA sequencing (scRNA-seq) data from the mouse cortex[14]. The results revealed that RNA editing at the GluA2 Q/R site was uniformly complete (>95%) in all neuronal cell types (Extended Data Fig. 1), which suggested that unedited GluA2 does not significantly contribute to CP-AMPAR expression in PV neurons. Validated antibodies against the major AMPAR subunits GluA1 and GluA2 (Extended Data Fig. 2) showed that PV neurons express GluA2 at roughly 60% of the levels of neighbouring CaMKIIα+ excitatory neurons in both mice (Extended Data Fig. 3a,b) and marmosets (Extended Data Fig. 3c,d). Conversely, GluA1 was expressed about 1.7-fold higher in PV neurons, which contributed to a reduced GluA2 to GluA1 ratio and abundant GluA2-deficient CP-AMPARs (Extended Data Fig. 3e–g).

Single-cell transcriptomics data[14] of AMPAR subunits matched the protein-level data, with PV neurons expressing *GRIA2* mRNA at about 40% of its level in excitatory neurons (VGLUT1+; Extended Data Fig. 4a), which indicated the occurence of transcriptional regulation of CP-AMPARs. SST interneurons, which share the same developmental origin (medial ganglionic eminence), also expressed reduced GluA2 levels[7]. However, VIP+ interneurons, which originate separately from the caudal ganglionic eminence, had *GRIA2* mRNA levels similar to excitatory neurons (Extended Data Fig. 4a). Motivated by the tightly correlated mRNA expression of AMPAR subunits (Extended Data Fig. 4d–g), we calculated the ratio of GluA2 to GluA1–GluA3–GluA4 subunits, which reflects the relative levels of calcium impermeable to permeable (R:Q) subunits, and found a similar ratio profile (Extended Data Fig. 4b). Notably, this ratio was always lowest in PV neurons across ferret, mouse, marmoset, macaque and human cortex datasets[27,28] (Extended Data Fig. 4h–l), which suggests that there is evolutionary pressure towards lower R:Q ratios specifically in these neurons. These results show that PV neurons across these species express GluA2 at a tightly regulated low expression stoichiometry, probably through a transcriptional mechanism that is strongest in PV neurons.

Manipulation of CP-AMPARs in PV neurons

To test the functional significance of low GluA2 and high CP-AMPAR expression, we used a recently generated transgenic mouse line[29] to express additional GluA2 with an eGFP tag in a Cre-dependent fashion (Extended Data Fig. 5). We crossed this transgenic mouse line with PV-Cre knock-in mice[30] to generate PV-Cre;lsl-eGFP-GluA2 mice (Fig. 1a). These mice strongly expressed GluA2 at the cell soma and along the dendrites of PV neurons (Extended Data Fig. 5b–d and Fig. 1b) at high concordance with PV immunofluorescence (Extended Data Fig. 5h–j). The transgenic expression of GluA2 led to PV interneurons with levels of GluA2 comparable to excitatory neurons, roughly twice the level of PV-Cre;lsl-eGFP control mice. This increased expression occurred both at the mRNA level (221.6 ± 26.9%) and protein level (217.2 ± 11.2%; Fig. 1b and Extended Data Fig. 5b–d), as revealed by FACS-assisted PV neuron RNA-seq (Methods) and immunohistochemistry, respectively. Notably, GluA1 protein (but not mRNA) expression was reduced in PV neurons expressing exogenous GluA2 (Fig. 1c and Extended Data Fig. 5e–g), similar to excitatory neuron levels, which suggested a post-transcriptional homeostatic or displacing effect. Transgenic expression of GluA2 in PV cells did not produce significant changes in PV or SST neuron density in the visual cortex (Extended Data Fig. 6).

Electrophysiological recordings revealed that the signature inward rectification of CP-AMPARs typical of PV neurons was absent in PV-Cre;lsl-eGFP-GluA2 mice (Fig. 1d and Extended Data Fig. 7a–f), which showed synaptic incorporation of calcium-impermeable AMPARs. These results confirm that the PV-Cre;lsl-eGFP-GluA2 mouse model is suitable for testing the functional role of CP-AMPARs in PV interneurons.

CP-AMPARs suppress PV selectivity

To test the role of CP-AMPARs in PV interneurons on sensory representation in awake mice, we assessed the orientation preference of layer 2/3 (L2/3) neurons in the V1 with in vivo two-photon (2P) calcium imaging (Fig. 1e). We injected PV-Cre;lsl-eGFP-GluA2 mice, PV-Cre;lsl-eGFP mice (controls) and CaMKIIα-Cre mice (as comparators) with a Cre-dependent jRGECO1a adeno-associated virus (AAV) targeting L2/3 of the visual cortex. Cranial windows were implanted on these mice and retinotopic mapping was performed to map the monocular V1 for 2P imaging (Extended Data Fig. 8a–e). We imaged somatic Ca^{2+} activity as a proxy for action potential activity during drifting grating presentation, focusing on the effect of neuronal firing rather than dendritic calcium dynamics. A proportion of PV neurons was visually responsive (Extended Data Fig. 8f) and displayed strong activity towards the 4-s presentations of full-field drifting gratings but not to blank isoluminant grey screen control trials (Fig. 1f). Consistent with previous observations[17–21], the orientation selectivity of L2/3 PV interneurons was lower than excitatory neurons (with considerable variability in both populations[4,22]). Selectivity was significantly enhanced when GluA2 expression was increased to match the level in excitatory neurons (Fig. 1g; $\chi_2^2 = 175.67$, $P < 0.0001$, Kruskal−Wallis one-way analysis of variance (ANOVA); $P < 0.0001$ for CaMKIIα-Cre versus PV-Cre;lsl-eGFP and for PV-Cre;lsl-eGFP versus PV-Cre;lsl-eGFP-GluA2, Dunn's multiple comparison correction). Despite distinct circuit underpinnings[4,15,16,19,31–33], direction selectivity was similarly enhanced, which indicated a general increase in selectivity as a result of CP-AMPAR removal (Fig. 1h; $\chi_2^2 = 50.76$, $P < 0.0001$, Kruskal−Wallis one-way ANOVA; $P = 0.0001$ for CaMKIIα-Cre versus PV-Cre;lsl-eGFP and for PV-Cre;lsl-eGFP versus PV-Cre;lsl-eGFP-GluA2). These observations remained significant in more stringent animal-level statistics (Extended Data Fig. 8k,l). The average response amplitude was not significantly changed in neuron-level comparisons (Extended Data Fig. 8g,n). The average tuning curve demonstrated how relative non-preferred stimuli responses were reduced in PV neurons without CP-AMPARs, which produced
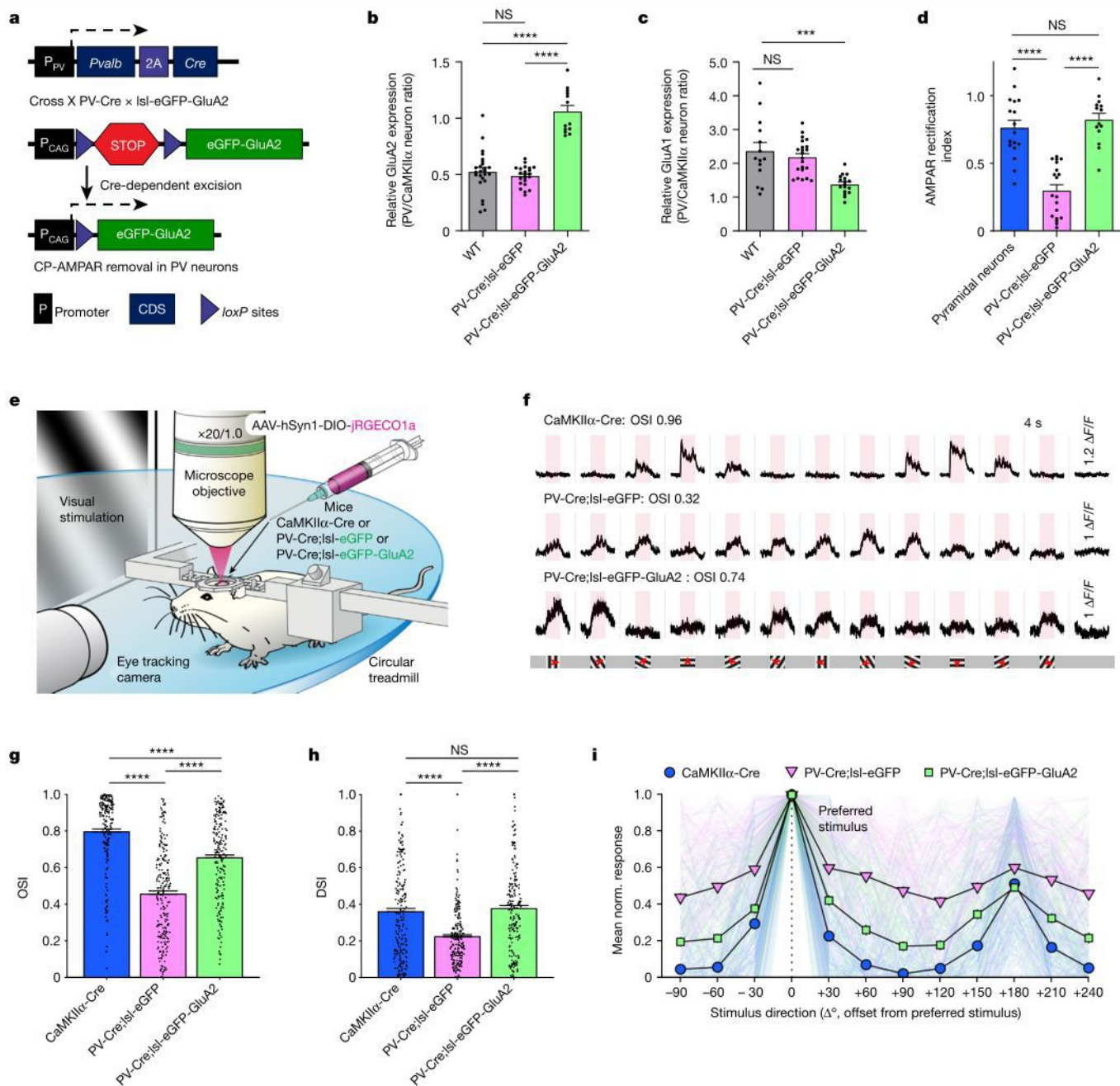
Fig. 1 | GluA2 expression in PV interneurons alters orientation selectivity in the L2/3 of the mouse visual cortex. a, Strategy to selectively remove CP-AMPARs in PV neurons. CDS, coding sequence. **b**, Relative GluA2 protein expression in PV and CaMKIIα neurons (left to right: $n = 25$, 22 and 13 pairs from 4, 4 and 4 slices, 3, 3 and 3 mice, respectively; $P = 3.961 \times 10^{-7}$, Kruskal–Wallis one-way ANOVA; $P < 0.0001$ for all PV-Cre;lsl-eGFP-GluA2 post hoc comparisons, Dunn's multiple comparison correction). NS, not significant; WT, wild type. **c**, Relative GluA1 expression (left to right: $n = 14$, 22 and 17 pairs from 3, 3 and 3 slices, 3, 3 and 3 mice, respectively; $P = 4.845 \times 10^{-5}$, one-way ANOVA; $P < 0.001$ for all eGFP-GluA2 group post hoc comparisons, Tukey's multiple comparison correction). Data are mean ± s.e.m. **d**, The low AMPAR rectification index in PV control neurons (lsl-eGFP, 0.298 ± 0.044) is increased in PV-Cre;lsl-eGFP-GluA2 mice (0.823 ± 0.047) to levels comparable with pyramidal neurons (0.763 ± 0.056) recorded for comparison (left to right: $n = 17$, 19 and 14 cells from 4, 3 and 2 mice, respectively; $P = 4.056 \times 10^{-10}$, one-way ANOVA test; $P < 0.0001$ for all post hoc comparisons with PV-Cre;lsl-eGFP mice, Tukey's multiple comparison correction), thereby indicating the removal of CP-AMPARs. **e**, Mice were head-fixed and visually stimulated during 2P imaging of the V1. **f**, Neuronal soma

activity traces. Pink rectangles denote the 4-s visual stimulation period and 1.2, 1.0 and 1.0 $\Delta F/F$ for each group. Grey shading corresponds to s.e.m. Whole screen drifting grating stimulation in 12 different directions was used to assess orientation selectivity. Red arrows mark the drifting direction. **g**, CaMKIIα neurons in CaMKIIα-Cre mice and PV neurons in PV-Cre;lsl-eGFP-GluA2 group displayed higher OSI values than in PV neurons in PV-Cre;lsl-eGFP controls (left to right: $n = 202$, 215 and 197 visually positive responsive neurons of 291, 316 and 395 total neurons from 3, 6 and 7 mice, respectively; $\chi^2_2 = 175.67$, $P = 7.154 \times 10^{-39}$, Kruskal–Wallis one-way ANOVA; $P < 0.0001$, Dunn's multiple comparison correction). **h**, The CaMKIIα-Cre group and the PV-Cre;lsl-eGFP-GluA2 group displayed higher direction selectivity index (DSI) values than the PV-Cre;lsl-eGFP controls ($\chi^2_2 = 50.76$, $P = 9.517 \times 10^{-12}$, Kruskal–Wallis one-way ANOVA; $P < 0.0001$). **i**, Normalized (norm.) average response profile of all positively responding neurons from each group aligned to their preferred stimulus direction (0°). A prominent peak is also present at +180° owing to the orientation selective nature of V1 neurons. Responses are plotted as the mean ± s.e.m.
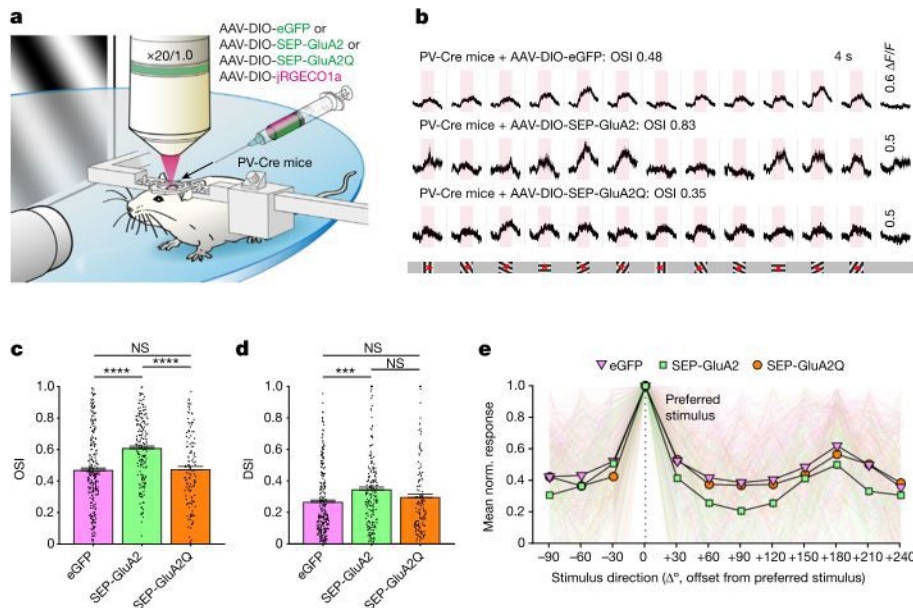
Fig. 2 | Sparse GluA2 expression in L2/3 PV interneurons increases their orientation and direction selectivity. a, Pre-injected mice were head-fixed and visually stimulated during 2P imaging of the V1 to reveal differences in tuning. **b**, Representative traces of neurons infected with AAV-DIO-eGFP or AAV-DIO-SEP-GluA2. Pink regions denote the 4-s visual stimulation period and 0.6, 0.5 and 0.5 $\Delta F/F$ for each group. Drifting grating stimulation was used to assess orientation selectivity. Red arrows mark the drifting direction. **c**, The SEP-GluA2 group displayed higher orientation selectivity than eGFP controls, whereas the SEP-GluA2Q group did not show increased OSI (left to right: $n = 252$, 184 and 132 visually responsive neurons of 325, 267 and 161 total

neurons from 7, 7 and 5 mice, respectively; $\chi_2^2 = 41.68$, $P = 8.892 \times 10^{-10}$, one-way ANOVA; $P < 0.0001$ for eGFP versus SEP-GluA2; $P = 0.9863$ for eGFP versus SEP-GluA2Q, Dunn's multiple comparison correction). **d**, Similarly, the SEP-GluA2 group displayed higher direction selectivity than the eGFP control group, whereas the SEP-GluA2Q group did not show higher DSI values ($P = 9.843 \times 10^{-4}$, $\chi_2^2 = 13.85$, Kruskal–Wallis one-way ANOVA; $P = 0.0006$ for eGFP versus SEP-GluA2; $P = 0.5195$ for eGFP versus SEP-GluA2Q). **e**, Normalized average response profile of all positively responding neurons aligned to their preferred stimulation (0°). Responses are plotted as the mean ± s.e.m.

increased orientation and direction selectivity (Fig. 1i and Extended Data Fig. 8h–j).

Cell-autonomous effect of CP-AMPAR removal

These results suggested that CP-AMPARs help reduce the visual feature selectivity of PV interneurons. To ask whether this effect arose from the systemic expression of GluA2 in PV neurons or from a cell-autonomous effect, we developed an AAV vector that sparsely expresses super-ecliptic pHluorin (SEP)-tagged GluA2 in a Cre-dependent fashion (Methods). Using this AAV-DIO-SEP-GluA2 virus, we observed strong expression of SEP-GluA2 in cultured neurons and in vivo (Extended Data Fig. 7g,h). As expected, rectification measurements demonstrated strong removal of CP-AMPARs in PV neurons compared with the control AAV-DIO-eGFP (Extended Data Fig. 7i–l). To further control for increased GluA2 expression, we used the calcium-permeable form of GluA2 (AAV-DIO-SEP-GluA2Q). This AAV similarly supplements GluA2 but should increase the proportion of CP-AMPARs. Indeed, this virus increased the rectification in PV neurons (Extended Data Fig. 7m).

Sparsely expressing GluA2 in PV neurons increased orientation selectivity, which suggested that the effect of CP-AMPAR removal is cell-autonomous (Fig. 2a–c and Extended Data Fig. 9; $\chi_2^2 = 41.68$, $P < 0.0001$, Kruskal–Wallis one-way ANOVA; $P < 0.0001$ for eGFP versus SEP-GluA2 orientation selectivity index (OSI), Dunn's multiple comparison correction). Notably, this effect was observed even in a >8-month-old mouse ($P < 0.0001$, Mann–Whitney U-test), a finding consistent with an ongoing role of CP-AMPARs in suppressing orientation selectivity. The calcium-permeable form of GluA2 (SEP-GluA2Q) did not increase PV neuron orientation selectivity ($P = 0.9863$ for eGFP versus SEP-GluA2Q), which suggested that channel pore calcium permeability has a specific role. Moreover, SEP-GluA2Q expression did

not lead to a decrease in orientation selectivity, which indicated a saturation or a floor effect.

Sparse SEP-GluA2 expression increased direction selectivity, whereas SEP-GluA2Q did not (Fig. 2d; $P = 0.0009$, $\chi_2^2 = 13.85$, Kruskal–Wallis one-way ANOVA; $P = 0.0006$ for eGFP versus SEP-GluA2; $P = 0.5195$ for eGFP versus SEP-GluA2Q), which suggested that CP-AMPARs are necessary for the low selectivity of PV neurons to various visual features. These changes in orientation and direction selectivity were replicated in stringent animal-level statistics (Extended Data Fig. 9g,h), but the proportion of visually responsive neurons and average response amplitude were not consistently different (Extended Data Fig. 9b,c,i,j). The average tuning curve confirmed reduced responses to non-preferred stimuli in SEP-GluA2-expressing PV neurons (Fig. 2e). Expression of the calcium-impermeable mutant GluA1 (GluA1(Q582R)) led to significantly higher orientation selectivity (but not direction selectivity) compared with wild-type GluA1 (Extended Data Fig. 9k). This result shows that R-form AMPAR subunits commonly increase orientation selectivity in PV neurons.

CP-AMPARs shape excitability but not connectivity

Excitatory neurons have a sparser input connectivity with local neurons than with PV neurons, which may underlie their higher orientation selectivity[33–36]. Thus, it is possible that dense local excitatory input connections of PV neurons become sparser following removal of CP-AMPARs to resemble excitatory neurons. Alternatively, the nominal connectivity rate may be unchanged, thereby implying that more specific mechanisms account for selectivity change. We used paired whole-cell patch-clamp recordings in acute brain slices to test the connectivity of L2/3 PV neurons and nearby excitatory neurons. We found no significant changes in the excitatory input or in reciprocal inhibitory output connection probability (Extended Data Fig. 10a–h).
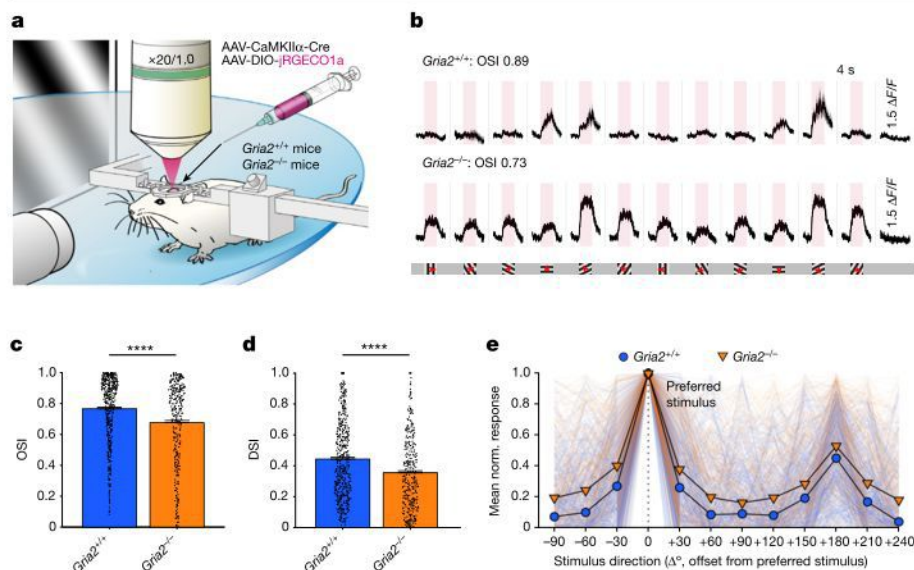
Fig. 3 | GluA2 homozygous knockout leads to decrease of selectivity in excitatory neurons. **a**, Pre-injected GluA2-knockout (*Gria2*⁻/⁻) and littermate wild-type (*Gria2*⁺/⁺) mice were head-fixed and visually stimulated during 2P imaging of the V1 to reveal differences in tuning. **b**, Representative traces of *Gria2*⁺/⁺ and *Gria2*⁻/⁻ excitatory neurons. Pink regions denote the 4-s visual stimulation period and 1.5 Δ*F/F* for both groups. Whole screen drifting grating stimulation with 12 different orientations was used to assess orientation selectivity. Red arrows mark the drifting direction. **c**, Quantification of orientation selectivity shows a significantly lower OSI in *Gria2*⁻/⁻ neurons than in wild-type controls (left to right: *n* = 504 and 340 from 3 and 3 mice, respectively; *P* = 8.733 × 10⁻⁷, Mann–Whitney *U*-test). **d**, The *Gria2*⁻/⁻ group also displayed lower direction selectivity (*P* = 3.552 × 10⁻⁷, Mann–Whitney *U*-test). **e**, Normalized average response profile of all positively responding neurons aligned to their preferred stimulation (0°). Responses are plotted as the mean ± s.e.m.

In connected pairs, the excitatory-to-PV neuron unitary excitatory postsynaptic potential (EPSP) amplitudes were not significantly reduced (Extended Data Fig. 10f), despite the loss of high-conductance CP-AMPARs, which suggests that there is a feedback or homeostatic mechanism that preserves synaptic strength. These results reject the idea that a large change in excitatory input connectivity is a mechanism for increasing orientation selectivity. However, they do not exclude the possibility that presynaptic input reorganization could lead to higher selectivity.

Input reorganization could arise from altered synaptic plasticity in PV neurons due to the removal of CP-AMPARs, which mediate an anti-Hebbian form of long-term potentiation (LTP) in hippocampal PV neurons through their ability to allow calcium influx at polarized potentials[25]. Synaptic plasticity has been underexplored in cortical PV neurons and generally presents as long-term depression (LTD) or smaller LTP compared with hippocampal neurons and excitatory neurons[37,38]. Consistently, several anti-Hebbian LTP induction protocols failed to result in potentiation in visual cortex PV neurons, instead leading to depression (Extended Data Fig. 10k–m). This LTD was exaggerated in PV-Cre;lsl-eGFP-GluA2 mice compared with control mice (*P* = 0.03968, unpaired *t*-test), which suggested that CP-AMPARs regulate the expression of non-Hebbian LTD in PV neurons.

Notably, PV neurons displayed markedly higher intrinsic excitability after CP-AMPAR removal, with a substantial increase in current-injected spike frequency, input resistance and action potential half-width, along with a decrease in rheobase and afterhyperpolarization (Extended Data Fig. 10n–v). Short action potential half-width, low input resistance and large afterhyperpolarization are all canonical features of PV neurons[5]. This finding suggests that removing CP-AMPARs led to a shift towards excitatory neuron-like intrinsic excitability characteristics. The resting membrane potential was also increased in PV-Cre;lsl-eGFP-GluA2 mice when measured without synaptic glutamate and GABA receptor blockers (Extended Data Fig. 10w), which suggested that there was a change in the balance of tonically active excitatory and inhibitory inputs (extrinsic synaptic excitability). Together, these results show that there is intact connectivity but altered synaptic plasticity and intrinsic excitability in PV neurons after removing CP-AMPARs.

Transcriptional response to CP-AMPAR removal

To investigate the new link between CP-AMPARs and excitability, we assessed global PV neuron transcriptome changes with fixation-capture single-cell RNA recovery sequencing (FICSR-seq; Methods) on forebrain PV neurons (Extended Data Fig. 11). FACS-assisted PV neuron bulk RNA-seq of PV-Cre;lsl-eGFP-GluA2 mice and PV-Cre;lsl-eGFP control mice showed no changes in expression in 278 out of 279 genes that constitute the major classes of ion channels and excitatory and inhibitory synapse proteins (Extended Data Figs. 12 and 13). This result points towards a post-transcriptional regulation of intrinsic and extrinsic (synaptic) excitability. The exception was *Gria2* mRNA, which was expressed about twofold higher than in control PV neurons (*P*_adjusted = 4.63 × 10⁻⁹, Benjamini–Hochberg correction; Extended Data Fig. 12), a result in agreement with protein measurements (Fig. 1b). GluA1, although downregulated at the protein level (Fig. 1c), was unchanged at the mRNA level. These transcriptomics results suggest that the substantial changes in PV neuron excitability after CP-AMPAR removal are not caused by changes in gene expression but probably reflect post-transcriptional regulation.

CP-AMPARs blunt excitatory selectivity

Removing CP-AMPARs from PV neurons renders them more selective. Therefore, we wondered whether introducing CP-AMPARs to excitatory neurons would reduce their orientation selectivity. To test this hypothesis, we assessed visual representation in GluA2 homozygous knockout mice, in which even excitatory neurons express abundant amounts of CP-AMPARs. Earlier studies[39,40] had established that hippocampal neurons of these mice have reduced AMPAR currents with complete inward rectification and altered synaptic plasticity, but the impact on sensory representation has not been reported.

Using a dual virus approach (Fig. 3a), we measured the visual responses of excitatory neurons (which typically have low CP-AMPAR levels) in GluA2-knockout mice (*Gria2*⁻/⁻) and littermate controls (*Gria2*⁺/⁺). Excitatory neurons in the *Gria2*⁻/⁻ mice displayed substantially reduced orientation selectivity (Fig. 3b,c,e; *P* < 0.0001, Mann–Whitney *U*-test) and direction selectivity (Fig. 3d,e; *P* < 0.0001, Mann–Whitney *U*-test). The proportion of visually responsive neurons and average response amplitude were not significantly different (Extended Data Fig. 14b,c). The change in direction selectivity did not reach significance in animal-level statistics, which suggests that the causal impact of CP-AMPARs on direction selectivity may be weaker than on orientation selectivity (Extended Data Fig. 14f,g). Non-preferred stimuli responses were relatively increased in excitatory neurons in the *Gria2*⁻/⁻ mice, which in turn led to decreased orientation and direction selectivity (Fig. 3e and Extended Data Fig. 14d,e). These results suggest
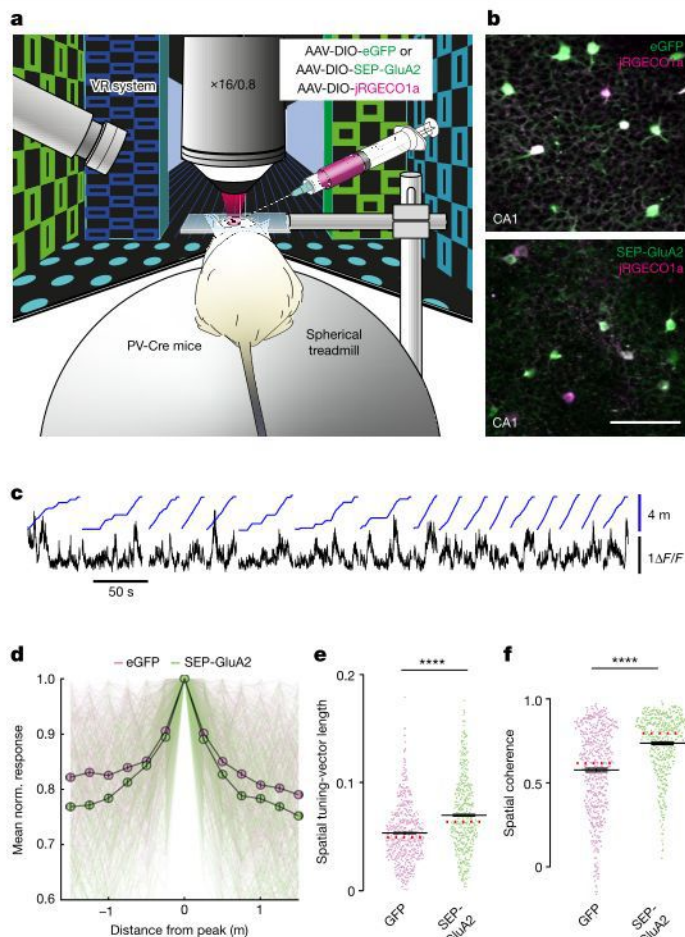
Fig. 4 | Increased spatial tuning of hippocampal PV interneurons after expression of GluA2. a, Experimental schematic of the virtual reality (VR) system. **b**, Time average of fluorescence acquired in vivo for jRGECO1a and SEP-GluA2 or eGFP. Scale bar, 100 μm. **c**, Ca^{2+} activity traces (black) and mouse position in virtual reality linear track (blue) over time. **d**, Normalized average spatial response profile of hippocampal CA1 PV neurons expressing SEP-GluA2 (green) or eGFP (magenta) aligned to the location of their peak activation. Responses are plotted as the mean ± s.e.m. Thin lines denote individual cells. **e**, Spatial tuning-vector lengths (Extended Data Fig. 15c) of PV neurons transfected with SEP-GluA2 were significantly higher than GFP controls (left to right: n = 583 and 476 cells from 4 and 4 mice, respectively; $P = 1.472 \times 10^{-14}$, Wilcoxon rank-sum test). **f**, Spatial coherence was also higher in the SEP-GluA2 group ($P = 1.532 \times 10^{-26}$, Wilcoxon rank-sum test). Black lines in **e** and **f** denote the mean ± s.e.m., and the red dotted line denotes the median. Dots denote values for individual cells.

that CP-AMPAR expression is sufficient to reduce selectivity regardless of neuron type.

Spatial selectivity of CA1 PV interneurons

We asked whether CP-AMPARs regulate PV interneuron selectivity beyond the visual cortex. PV neurons in the hippocampus have lower spatial selectivity than their neighbouring pyramidal cells[3,5], but the molecular mechanisms underlying this reduced selectivity are unknown.

Using a virtual navigation task in head-fixed animals[41] (Fig. 4a and Methods), in which mice are running on a 4-m-long virtual linear track, we imaged hundreds of PV neurons in the CA1 of PV-Cre mice transfected with Cre-dependent AAV expressing SEP-GluA2 or eGFP as a control (Fig. 4b). We previously measured reliable place fields of excitatory neurons with this experimental set up[41], which indicated

that the hippocampus forms a strong internal representation of the virtual environment.

Notably, we observed that the activity of SEP-GluA2-expressing PV neurons (Fig. 4c) was more sharply tuned to the preferred location than GFP-expressing control PV neurons (Fig. 4d). This was reflected in increases in spatial tuning-vector length (Fig. 4e and Extended Data Fig. 15c), spatial coherence (local smoothness of the spatial tuning curve; Fig. 4f) spatial information and within-session stability of spatial tuning curves, and decreases in variability of spatial responses between trials (Extended Data Fig. 15b,f,e). In summary, these data suggest that GluA2-deficient CP-AMPARs reduce the selectivity of PV neurons regardless of modality and have a broad role in sensory representation beyond the neocortex.

Computational modelling of CP-AMPAR removal

Given the electrophysiological changes we observed with CP-AMPAR removal, we used computational models to identify which mechanisms are consistent with the increase in feature selectivity. We explored the following three electrophysiological circuit changes: (1) increased intrinsic excitability, (2) the loss of inward-rectifying AMPAR current and (3) enhanced LTD. We used a model comprising a single PV neuron receiving a set of inputs from presynaptic excitatory neurons with predefined stimulus tuning (Fig. 5a). To endow the PV neuron with stimulus tuning, the strength of excitatory–PV synapses was modelled as bell-shaped around the preferred orientation of PV neurons (Fig. 5b), which enabled PV neurons to inherit their tuning from pyramidal cells (Fig. 5c).

First, we found that implementing increased PV neuron intrinsic excitability alone could not account for the observed increase in stimulus selectivity. In fact, it reduced selectivity by increasing the response of the neuron to all stimuli (Extended Data Fig. 16a–h). Notably, the inward-rectifying nature of the CP-AMPAR ion channel effectively dampened excitatory transmission during strong responses compared with weak responses across a wide range of conditions (Fig. 5d–g and Extended Data Fig. 16i–n). Last, when we incorporated exaggerated LTD, this preferentially weakened synapses from excitatory neurons that elicited weak responses in the PV neuron (Fig. 5i). Both the removal of inward rectification and the exaggerated LTD reduced responses to non-preferred stimuli relative to the preferred stimuli (Figs. 2e and 5e,j), which accounted for the increases in orientation selectivity. These modelling studies suggest that both acute rectification and cumulative plasticity triggered by resident CP-AMPARs in PV neuron dendrites may sufficiently account for their role in maintaining low selectivity (Extended Data Fig. 17).

Discussion

Our results showed that CP-AMPARs are both necessary for low orientation selectivity in PV interneurons and sufficient to induce reduced selectivity in excitatory neurons, which typically have few CP-AMPARs. The function of postsynaptic AMPARs in synaptic transmission and defining synaptic strength is well understood[9,10,24]. Our new results suggest that their biophysical properties can control neuronal response tuning, thereby expanding their active role in computation. Whereas CP-AMPARs have been extensively studied in excitatory neuron synapses, our results attributed a new function to forebrain CP-AMPARs, which overwhelmingly reside in inhibitory neurons.

Our findings have broad implications for understanding inhibitory architecture. Inhibitory PV interneurons provide rapid feedback inhibition to local excitatory neurons. This lateral inhibition constrains the timing and extent of their firing while reducing informational redundancy[5,12]. The selectivity of PV neuron activity compared with excitatory neurons[17–22] and the tuning bias of their outputs on local excitatory neurons[31,34,35,42–44] have been under debate. Here we showed that the
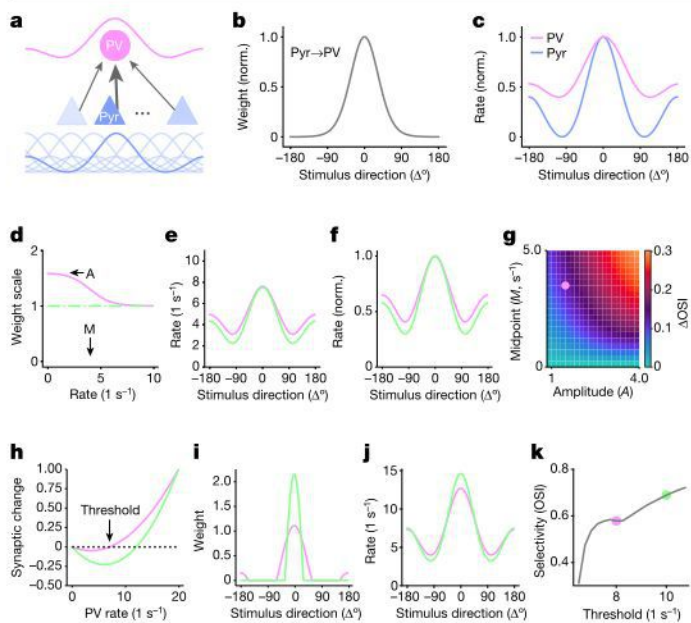
Fig. 5 | Mathematical models of the impact of CP-AMPAR removal on selectivity. a, Feed-forward network architecture of a PV neuron (circle) receiving inputs from pyramidal cells (Pyr; triangles, $n = 64$). Insets depict tuning curves. **b**, Pyramidal–PV connectivity depends on the difference between the preferred orientation of the PV neuron and the pyramidal cell in question. **c**, Tuning of pyramidal and PV responses. OSI: 0.73 (Pyr) and 0.44 (PV). Rates are normalized by their maximum for visual comparison. **d**, Rate-dependent weight reduction as a model of CP-AMPAR-dependent inward rectification in control PV-Cre;lsl-eGFP neurons (magenta), parametrized by a maximum amplitude A and a midpoint M. The removal of CP-AMPARs and inward rectification in PV-Cre;lsl-eGFP-GluA2 mice is modelled by removing the rate dependence of the synaptic weights (green). **e**, Removal of CP-AMPARs decreases responses to non-preferred stimuli but not to preferred stimuli, thereby increasing stimulus selectivity. OSI with and without CP-AMPARs: 0.48 and 0.59, respectively. **f**, As for **e**, but normalized. **g**, Orientation selectivity increases for most combinations of amplification and midpoint. Dot shows the example shown in **e** and **f** ($A = 1.6$, $M = 4$). **h**, Bienenstock–Cooper–Munro plasticity rule. PV rates below the threshold cause LTD, whereas PV rates above the threshold cause LTP. Exaggerated LTD is modelled by increasing the threshold (magenta, 8 Hz; green, 12 Hz). **i**,**j** Increased LTD sharpens the pyramidal–PV connectivity (**i**) and increases PV selectivity (**j**). OSI with baseline and increased LTD: 0.58 and 0.69, respectively. **k**, Orientation selectivity increases with the threshold as long as this threshold is within the range of PV responses (between about 6 and 11 Hz).

reduced selectivity of these PV neurons is biophysically implemented with a well-conserved molecular mechanism, including transcriptional *Gria2* downregulation.

Whether other mammalian and non-mammalian organisms share such molecular or computational architecture is a question that needs investigation, and answers may reveal how molecular motifs that enable computation have evolved. It is notable that even PV-like GABAergic neurons in evolutionarily distant lizards, which lack *Pvalb* expression, also display low *Gria2* expression[45]. Conversely, the importance of low CP-AMPAR expression in excitatory neurons has been highlighted by the discovery of human heterozygous de novo *GRIA2* mutations through whole-genome sequencing efforts[46]. Mutations that lead to *GRIA2* loss of function or remove the calcium-blocking pore residue of *GRIA2* are often associated with intellectual disability and autistic behaviours, which suggests that the tight control of AMPAR calcium permeability is essential for human cognition.

In a given brain area, neurons display varying levels of selectivity to their preferred stimulus set. This selectivity can be stratified along the line of neuronal cell types[12,16,47]. This diversity indicates that gene expression can significantly affect the selectivity and sensory representation of a given neuron. Because synaptic inputs are summed in space and time to trigger neuronal activity, the selectivity of a neuron is dictated by the functional bias of the synaptic input pool[31], the organization of the input synapses along the dendritic structure and the intrinsic excitability of each neuron.

Previous studies have suggested that PV neurons have low selectivity because they receive high-density excitatory input from cells with diverse tuning features and low overall functional bias[20,33–36]. Our paired recordings showed that gross input connectivity rates are intact in mice when PV neuron CP-AMPARs are removed, thereby demonstrating that PV neuron orientation selectivity can increase without significantly changing connection rates. However, these recordings did not address whether the functional bias of input connections or the clustering of such synapses throughout the dendritic tree is altered by the lack of CP-AMPARs. Thus, anti-Hebbian plasticity may have a role in the dendritic organization of functionally tuned synapses. The inward rectification of CP-AMPARs may limit strong functional summation from a particular dendrite or presynaptic partner, thereby further contributing to broader tuning. Meanwhile, our results showed that the intrinsic excitability of PV neurons is tightly coupled to the AMPAR profile, which implicates interleaved and coordinated mechanisms that define the computation of a given neuron. It is possible that blocking a key Ca^{2+} input source in dendrites by removing CP-AMPARs leads to a homeostatic response in PV neurons to upregulate excitability[48]. Intrinsic excitability is specifically adapted in PV neurons[5], and how this tightly regulated feature of PV neurons affects its computations remains an essential question for future studies.

It is interesting to consider what these results tell us about biological and in silico intelligent circuits. Hebbian plasticity in neuronal networks is predicted to increase the correlation between neuronal activity and degrade total information content[2]. Anti-Hebbian plasticity is a possible mechanism to counteract this by reducing redundancy and keeping the representation more independent. However, researchers have traditionally thought that anti-Hebbian plasticity is implemented at the output GABAergic synapses of the inhibitory network[2,49]. By contrast, our work showed that CP-AMPARs at the input of the inhibitory network reduce GABAergic selectivity, thereby allowing PV neurons to broadly inhibit correlated activity through lateral inhibition. This characteristic adds to the flexibility of the network and may contribute to the canonical normalization computation that PV neurons are thought to carry out[50]. How the increased feature selectivity of PV neurons after CP-AMPAR removal affects local neuronal population coding and broader cognition are important outstanding questions.

We described a mechanism that commonly governs PV neuron selectivity across multiple modalities, from orientation and direction selectivity in the visual cortex to spatial selectivity in the hippocampus. By no means did we exhaustively assess the selectivity of these neurons in other domains, such as colour, ocular dominance and speed[4,15,19,21,31]. Selectivity to some visual features emerges before visual experience at eye-opening and can be driven by genetically determined circuit formation[15]. Future studies will show how experience-dependent synaptic regulation through CP-AMPARs and other synaptic molecules interacts with genetically determined mechanisms to fine-tune sensory representation.

Online content

Any methods, additional references, Nature Portfolio reporting summaries, source data, extended data, supplementary information, acknowledgements, peer review information; details of author contributions and competing interests; and statements of data and code availability are available at https://doi.org/10.1038/s41586-024-08027-2.

1. Olshausen, B. A. & Field, D. J. Sparse coding of sensory inputs. *Curr. Opin. Neurobiol.* **14**, 481–487 (2004).
2. Destexhe, A. & Marder, E. Plasticity in single neuron and circuit computations. *Nature* **431**, 789–795 (2004).
3. Moser, M. B., Rowland, D. C. & Moser, E. I. Place cells, grid cells, and memory. *Cold Spring Harb. Perspect. Biol.* **7**, a021808 (2015).
4. Niell, C. M. Cell types, circuits, and receptive fields in the mouse visual cortex. *Annu. Rev. Neurosci.* **38**, 413–431 (2015).
5. Hu, H., Gan, J. & Jonas, P. Interneurons. Fast-spiking, parvalbumin⁺ GABAergic interneurons: from cellular design to microcircuit function. *Science* **345**, 1255263 (2014).
6. Huang, Z. J. & Paul, A. The diversity of GABAergic neurons and neural communication elements. *Nat. Rev. Neurosci.* **20**, 563–572 (2019).
7. Matta, J. A. et al. Developmental origin dictates interneuron AMPA and NMDA receptor subunit composition and plasticity. *Nat. Neurosci.* **16**, 1032–1041 (2013).
8. Petersen, C. C. & Crochet, S. Synaptic computation and sensory processing in neocortical layer 2/3. *Neuron* **78**, 28–48 (2013).
9. Huganir, R. L. & Nicoll, R. A. AMPARs and synaptic plasticity: the last 25 years. *Neuron* **80**, 704–717 (2013).
10. Malinow, R. & Malenka, R. C. AMPA receptor trafficking and synaptic plasticity. *Annu. Rev. Neurosci.* **25**, 103–126 (2002).
11. Zeng, H. & Sanes, J. R. Neuronal cell-type classification: challenges, opportunities and the path forward. *Nat. Rev. Neurosci.* **18**, 530–546 (2017).
12. Fishell, G. & Kepecs, A. Interneuron types as attractors and controllers. *Annu. Rev. Neurosci.* **43**, 1–30 (2020).
13. Paul, A. et al. Transcriptional architecture of synaptic communication delineates GABAergic neuron identity. *Cell* **171**, 522–539.e20 (2017).
14. Tasic, B. et al. Adult mouse cortical cell taxonomy revealed by single cell transcriptomics. *Nat. Neurosci.* **19**, 335–346 (2016).
15. Seabrook, T. A., Burbridge, T. J., Crair, M. C. & Huberman, A. D. Architecture, function, and assembly of the mouse visual system. *Annu. Rev. Neurosci.* **40**, 499–538 (2017).
16. Isaacson, J. S. & Scanziani, M. How inhibition shapes cortical activity. *Neuron* **72**, 231–243 (2011).
17. Sohya, K., Kameyama, K., Yanagawa, Y., Obata, K. & Tsumoto, T. GABAergic neurons are less selective to stimulus orientation than excitatory neurons in layer II/III of visual cortex, as revealed by in vivo functional Ca²⁺ imaging in transgenic mice. *J. Neurosci.* **27**, 2145–2149 (2007).
18. Nowak, L. G., Sanchez-Vives, M. V. & McCormick, D. A. Lack of orientation and direction selectivity in a subgroup of fast-spiking inhibitory interneurons: cellular and synaptic mechanisms and comparison with other electrophysiological cell types. *Cereb. Cortex* **18**, 1058–1078 (2008).
19. Liu, B. H. et al. Visual receptive field structure of cortical inhibitory neurons revealed by two-photon imaging guided recording. *J. Neurosci.* **29**, 10520–10532 (2009).
20. Kerlin, A. M., Andermann, M. L., Berezovskii, V. K. & Reid, R. C. Broadly tuned response properties of diverse inhibitory neuron subtypes in mouse visual cortex. *Neuron* **67**, 858–871 (2010).
21. Niell, C. M. & Stryker, M. P. Highly selective receptive fields in mouse visual cortex. *J. Neurosci.* **28**, 7520–7536 (2008).
22. Runyan, C. A. et al. Response features of parvalbumin-expressing interneurons suggest precise roles for subtypes of inhibition in visual cortex. *Neuron* **67**, 847–857 (2010).
23. Geiger, J. R. et al. Relative abundance of subunit mRNAs determines gating and Ca²⁺ permeability of AMPA receptors in principal neurons and interneurons in rat CNS. *Neuron* **15**, 193–204 (1995).
24. Traynelis, S. F. et al. Glutamate receptor ion channels: structure, regulation, and function. *Pharmacol. Rev.* **62**, 405–496 (2010).
25. Lamsa, K. P., Heeroma, J. H., Somogyi, P., Rusakov, D. A. & Kullmann, D. M. Anti-Hebbian long-term potentiation in the hippocampal feedback inhibitory circuit. *Science* **315**, 1262–1266 (2007).
26. Gu, J. G., Albuquerque, C., Lee, C. J. & MacDermott, A. B. Synaptic strengthening through activation of Ca²⁺-permeable AMPA receptors. *Nature* **381**, 793–796 (1996).
27. Lake, B. B. et al. Neuronal subtypes and diversity revealed by single-nucleus RNA sequencing of the human brain. *Science* **352**, 1586–1590 (2016).
28. Krienen, F. M. et al. Innovations present in the primate interneuron repertoire. *Nature* **586**, 262–269 (2020).
29. Khawaja, R. R. et al. GluA2 overexpression in oligodendrocyte progenitors promotes postinjury oligodendrocyte regeneration. *Cell Rep.* **35**, 109147 (2021).
30. Hippenmeyer, S. et al. A developmental switch in the response of DRG neurons to ETS transcription factor signaling. *PLoS Biol.* **3**, e159 (2005).
31. Scholl, B., Thomas, C. I., Ryan, M. A., Kamasawa, N. & Fitzpatrick, D. Cortical response selectivity derives from strength in numbers of synapses. *Nature* **590**, 111–114 (2021).
32. Rossi, L. F., Harris, K. D. & Carandini, M. Spatial connectivity matches direction selectivity in visual cortex. *Nature* **588**, 648–652 (2020).
33. Scholl, B., Pattadkal, J. J., Dilly, G. A., Priebe, N. J. & Zemelman, B. V. Local integration accounts for weak selectivity of mouse neocortical parvalbumin interneurons. *Neuron* **87**, 424–436 (2015).
34. Hofer, S. B. et al. Differential connectivity and response dynamics of excitatory and inhibitory neurons in visual cortex. *Nat. Neurosci.* **14**, 1045–1052 (2011).
35. Bock, D. D. et al. Network anatomy and in vivo physiology of visual cortical neurons. *Nature* **471**, 177–182 (2011).
36. Packer, A. M. & Yuste, R. Dense, unspecific connectivity of neocortical parvalbumin-positive interneurons: a canonical microcircuit for inhibition? *J. Neurosci.* **31**, 13260–13271 (2011).
37. Lu, J. T., Li, C. Y., Zhao, J. P., Poo, M. M. & Zhang, X. H. Spike-timing-dependent plasticity of neocortical excitatory synapses on inhibitory interneurons depends on target cell type. *J. Neurosci.* **27**, 9711–9720 (2007).
38. Le Duigou, C., Savary, E., Kullmann, D. M. & Miles, R. Induction of anti-Hebbian LTP in CA1 stratum oriens interneurons: interactions between group I metabotropic glutamate receptors and M1 muscarinic receptors. *J. Neurosci.* **35**, 13542–13554 (2015).
39. Jia, Z. et al. Enhanced LTP in mice deficient in the AMPA receptor GluR2. *Neuron* **17**, 945–956 (1996).
40. Meng, Y., Zhang, Y. & Jia, Z. Synaptic transmission and plasticity in the absence of AMPA glutamate receptor GluR2 and GluR3. *Neuron* **39**, 163–176 (2003).
41. Hainmueller, T. & Bartos, M. Parallel emergence of stable and dynamic memory engrams in the hippocampus. *Nature* **558**, 292–296 (2018).
42. Znamenskiy, P. et al. Functional specificity of recurrent inhibition in visual cortex. *Neuron* **112**, 991–1000.e8 (2024).
43. Karnani, M. M., Agetsuma, M. & Yuste, R. A blanket of inhibition: functional inferences from dense inhibitory connectivity. *Curr. Opin. Neurobiol.* **26**, 96–102 (2014).
44. Yoshimura, Y. & Callaway, E. M. Fine-scale specificity of cortical networks depends on inhibitory cell type and connectivity. *Nat. Neurosci.* **8**, 1552–1559 (2005).
45. Tosches, M. A. et al. Evolution of pallium, hippocampus, and cortical cell types revealed by single-cell transcriptomics in reptiles. *Science* **360**, 881–888 (2018).
46. Salpietro, V. et al. AMPA receptor GluA2 subunit defects are a cause of neurodevelopmental disorders. *Nat. Commun.* **10**, 3094 (2019).
47. Bugeon, S. et al. A transcriptomic axis predicts state modulation of cortical interneurons. *Nature* **607**, 330–338 (2022).
48. Debanne, D., Inglebert, Y. & Russier, M. Plasticity of intrinsic neuronal excitability. *Curr. Opin. Neurobiol.* **54**, 73–82 (2019).
49. Pehlevan, C., Hu, T. & Chklovskii, D. B. A Hebbian/anti-Hebbian neural network for linear subspace learning: a derivation from multidimensional scaling of streaming data. *Neural Comput.* **27**, 1461–1495 (2015).
50. Carandini, M. & Heeger, D. J. Normalization as a canonical neural computation. *Nat. Rev. Neurosci.* **13**, 51–62 (2011).

¹The Solomon H. Snyder Department of Neuroscience, Johns Hopkins University School of Medicine, Baltimore, MD, USA. ²Kavli Neuroscience Discovery Institute, Johns Hopkins University, Baltimore, MD, USA. ³Department of Psychiatry and Behavioral Sciences, Johns Hopkins University School of Medicine, Baltimore, MD, USA. ⁴Emotion, Cognition and Behavior Research Group, Korea Brain Research Institute (KBRI), Daegu, Republic of Korea. ⁵Institute for Physiology I, University of Freiburg, Medical Faculty, Freiburg, Germany. ⁶Modelling of Cognitive Processes, Technical University of Berlin, Berlin, Germany. ⁷Charité–Universitätsmedizin Berlin, Einstein Center for Neurosciences Berlin, Berlin, Germany. ⁸Section on Cognitive Neurophysiology and Imaging, National Institute of Mental Health, Bethesda, MD, USA. ⁹Department of Brain and Cognitive Sciences, Korea Advanced Institute of Science and Technology (KAIST), Daejeon, Republic of Korea. ¹⁰Lieber Institute for Brain Development, Johns Hopkins Medical Campus, Baltimore, MD, USA. ¹¹Department of Neurology, Johns Hopkins University School of Medicine, Baltimore, MD, USA. ¹²Chica and Heinz Schaller Research Group, Institute for Anatomy and Cell Biology, Heidelberg, Germany. ¹³Interdisciplinary Center for Neurosciences, University of Heidelberg, Heidelberg, Germany. ¹⁴Princeton Neuroscience Institute, Princeton University, Princeton, NJ, USA. ¹⁵Department of Genetics, Harvard Medical School, Boston, MA, USA. ¹⁶Howard Hughes Medical Institute, Johns Hopkins University School of Medicine, Baltimore, MD, USA. ¹⁷Department of Ophthalmology, Johns Hopkins University School of Medicine, Baltimore, MD, USA. ¹⁸Institute for Cell Engineering, Johns Hopkins University School of Medicine, Baltimore, MD, USA. ¹⁹Bernstein Center for Computational Neuroscience Berlin, Berlin, Germany. ²⁰Science of Intelligence, Research Cluster of Excellence, Berlin, Germany. ²¹Present address: Department of Psychiatry, New York University Langone Medical Center, New York, NY, USA. ²²Present address: Danish Research Institute of Translational Neuroscience (DANDRITE), Nordic EMBL Partnership for Molecular Medicine, Aarhus University, Aarhus, Denmark. ²³Present address: Department of Biomedicine, Aarhus University, Aarhus, Denmark. ²⁴Present address: Center of Research Excellence in Allergy and Immunology, Research Department, Faculty of Medicine Siriraj Hospital, Mahidol University, Bangkok, Thailand. ²⁵These authors contributed equally: Ingie Hong, Juhyun Kim, Thomas Hainmueller. ✉e-mail: ingiehong@jhmi.edu; rhuganir@jhmi.edu

Article

Methods

Mice and marmosets

All procedures were approved by the Johns Hopkins Animal Care and Use Committee and conducted per the guidelines of the National Institutes of Health and the Society for Neuroscience. Hippocampal imaging experiments were carried out according to German national and institutional guidelines and approved by the 'Tierversuchskommission' of the Regierungspräsidium Freiburg (license number G16/037). Marmoset post-mortem tissue was obtained from terminal experiments approved by NIH Institutional Animal Care and Use Committees. The following mouse lines were used: PV-Cre[30] (Jackson Laboratory (JAX), 008069), lsl-eGFP[51] (JAX, 010701), lsl-eGFP-GluA2 (Extended Data Fig. 5), GluA2 KO[39] (JAX, 002913), and GluA1 KO[52] (JAX, 024422). We generated the ROSA26-lsl-eGFP-GluA2 mouse line by electroporating mouse embryonic stem (ES) cells with an engineered construct containing ROSA26-CAG-*loxP*-STOP-*loxP*-eGFP-Gria2-WPRE (adapted from targeting vector used to generate Ai14 mice[53]) and homologous recombination (Extended Data Fig. 5). We generated PV-Cre;lsl-eGFP-GluA2 (and PV-Cre;lsl-eGFP) mice from crosses with PV-Cre mice, born at Mendelian ratios. *GluA2*$^{-/-}$ pups displayed lower body weight compared with wild-type littermates. They displayed occasional mortality, mitigated by separating the littermates from the parents to reduce litter sizes[39]. All lines were maintained on a mixed background composed primarily of C57BL/6J, and mice of both sexes were used for experiments. We maintained all animals on a 12-h light–dark cycle at 20–26 °C and 30–70% relative humidity.

Constructs

We used Q/R and R/G RNA-edited flip-isoform short c-tail rat *Gria2* cDNA sequences for mutant animal generation and viruses unless otherwise stated. SEP-GluA2 and GFP-GluA2 fusion constructs were generated by amino-terminal insertion of SEP or GFP at four amino acids after the signal peptide padded with linker sequences, as in previously published constructs[54]. We generated the FUW-Cre construct by replacing the eGFP in FUGW with the Cre recombinase gene.

pAAV.Syn.Flex.NES-jRGECO1a.WPRE.SV40 (ref. 55) was a gift from D. Kim and the GENIE Project (Addgene, plasmid 100853). The *loxP*/lox2272 sequences in the Flex cassette were inverted or exchanged with lox511/loxFAS to mitigate compatibility with other DIO AAVs. pAAV-CW3SL-eGFP[56] was a gift from B.-K. Kaang (Addgene, plasmid 61463).

To deliver large genes, such as the SEP-GluA2 fusion gene, with the high tropism and low cytotoxicity provided by AAV vectors, we heavily optimized vector components to allow larger transgene size. Using the short hSyn1 promoter (469 bp), abbreviated linker sequences and DIO sequences and an optimized WPRE+polyA signal (CW3SL, 425 bp)[56], we generated a pan-neuronal Cre-dependent AAV expression vector with a minimal backbone (1,350 bp from inverted terminal repeat (ITR) to ITR without cargo) and large cargo capacity size (about 3.65 kb; based on an earlier estimation of 5 kb AAV genome size limit[57]; 3.85 kb when Cre dependency is not required). The *loxP*/lox2272 sites were spaced by a minimal 64 bp (5′ end-to-5′ end) to set the second recombination event distance (128 bp) above 118 bp, at which inefficient recombination has been reported, but at an exact multiple of the helical repeat length (10.6 bp). This repeat length allowed better-aligned *loxP* sites after DNA looping, thereby maximizing the efficiency of Cre-mediated excision[58].

As proof of principle, this study showed that SEP-GluA2 (3,378 bp), a large fusion protein previously only expressed through electroporation or lentiviral transfection, can be strongly expressed with this vector both in vitro and in vivo (Extended Data Fig. 7). The DIO-SEP-GluA2Q vector harboured *Gria2* cDNA unedited at the Q/R editing site (R607Q)[59]. GluA2 Q/R RNA editing occurs at the pre-mRNA stage and requires a hairpin structure in the adjacent intron, which is absent in this vector. This structure bypasses RNA editing and expression of a calcium-permeable GluA2Q subunit. The DIO-eGFP control virus was similarly generated, replacing SEP-GluA2 with eGFP, for use as a control. These plasmids have been deposited to Addgene for distribution to the scientific community.

AAV was produced by HHMI-Janelia Viral Tools using a PEI triple transfection protocol into AAV293T cells (an ITR-containing plasmid, 2/9 capsid helper from UPenn Vector Core and the E1-deleted pHelper plasmid from Agilent). The cells were grown under serum-free conditions (three 150 mm culture dishes at about 3×10^7 cells per dish for each 100 µl batch), purified by two rounds of CsCl density gradient centrifugation and exchanged into storage buffer (1× PBS, 5% sorbitol and 350 mM NaCl). Virus titres (GC per ml) were determined by qPCR targeting the AAV ITRs.

Stereotaxic cranial surgeries

We used stereotaxic surgery to inject viruses and to implant 4 mm square cranial windows over the left V1. Mice of mixed sex (>6 weeks old) were given carprofen (5 mg kg^{-1}) or buprenorphine (sustained release; 0.5–1.0 mg kg^{-1}) and dexamethasone (4 mg kg^{-1}) for analgesia and were anaesthetized using avertin or isoflurane (1.5–2.5%). We made a craniotomy with a number 11 scalpel blade centred at 2.5 mm lateral and 3.4 mm posterior to bregma.

For AAV injections, viruses were diluted with sterile PBS to 1–5 × 10^{13} GC per ml. We injected the solution at 5–10 sites spanning the posterior central area of the craniotomy (corresponding to the V1) with about 100 nl injections at each site at 250 µm below the dura surface. Injections were made using a bevelled glass pipette and a custom mineral oil-based injection system over 2–4 min. We left the pipette in place for another 2–3 min to allow diffusion and to prevent backflow.

We placed a 4 mm square glass coverslip over the craniotomy and attached a stainless-steel head bar to the skull during surgery to allow rigid head-fixation during imaging. We allowed mice to recover for 1–2 weeks before imaging and handled them extensively to alleviate experiment-related stress.

For hippocampal experiments, virus injections and cortical excavation or window implantation were done in separate surgeries. We made a small craniotomy over the hippocampus and injected 500 nl of AAV into the CA1 (anterior–posterior (AP): −2.0 mm; medial–lateral (ML) 2.0 mm; dorsal–ventral (DV): −1.4 mm). In the same surgical session, we implanted mice with a stainless-steel head plate (25 × 10 × 0.8 mm with an 8 mm central aperture) horizontally. We allowed mice to recover from surgery for at least 5 days before training sessions. We continued postoperative analgesic treatment with carprofen (5 mg kg^{-1} body weight) for 3 days after surgery.

Cortical excavation and hippocampal imaging window implantation were performed >10 days after the initial virus injection per published protocols[41]. We made a craniotomy (diameter 3 mm) centred at AP −1.5 mm and ML −1.5 mm. Parts of the somatosensory cortex and posterior parietal association cortex were gently aspirated while irrigating with chilled saline. We continued aspiration until the external capsule was exposed. We then gently peeled away the outer part of the external capsule using fine forceps, leaving the inner capsule and the hippocampus undamaged. The imaging window implant consisted of a 3 mm diameter coverslip (CS-3R, Warner Instruments) glued to the bottom of a stainless-steel cannula (3 mm diameter 1.2–1.5 mm height). The window was gradually lowered into the craniotomy using forceps until the glass was in contact with the external capsule. The implant was then affixed to the skull using cyanoacrylate. We allowed mice to recover from window implantation for 2–3 days.

Awake in vivo 2P fluorescence imaging

We performed retinotopic mapping[60,61] to verify the location of the V1 using optimized protocols and software (https://github.com/ingiehong/retinotopy). We conducted awake in vivo 2P imaging with a custom-built, resonant/galvo 2P laser-scanning microscope

(Sutter Instrument) controlled by ScanImage (Vidrio Technologies) and light-proofed to allow imaging in ambient light during visual stimulation. The designs for the head-fixed imaging platform and lightproofing apparatus are available online (https://github.com/ingiehong/StackGPS). We imaged neurons in the L2/3 of monocular V1 expressing eGFP or SEP and jRGECO1a using a ×20/1.0 NA water-immersion objective (Zeiss) and a Ti:Sapphire laser (Coherent Chameleon Ultra; Spectra-Physics Insight X3) tuned at 930 nm or 1,040 nm, respectively, with 20–100 mW of power delivered to the back-aperture of the objective.

We corrected the lateral motion of acquired image sequences using a rigid motion correction algorithm (NoRMCorre[62]). Neuronal somata with calcium transients were segmented using a constrained non-negative matrix factorization algorithm[63]. The source-separated GCaMP or jRGECO1a signal from each neuron was used to estimate various visual response properties of L2/3 neurons.

Visual stimulation

Visual stimuli were presented on a gamma-corrected 27″ LED monitor placed 22 cm in front of the centre of the eye contralateral to the hemisphere in which imaging was performed. The visual stimuli consisted of full-screen drifting gratings (4 s of duration, sinusoidal, 0.05 cycles per degree, 1 Hz, 100% contrast) following a 4-s iso-luminant grey screen. Six orientation gratings spaced at 30° were presented drifting in both directions orthogonal to the gratings (total of 12 directions) in a pseudo-randomized order to characterize sensory tuning using Psychtoolbox-3 (ref. 64) and FocusStack/Stimserver[65]. We used the average response during the 4 s of stimuli across 9–11 presentations to calculate visual responsiveness and orientation and direction selectivity. Visually responsive neurons were defined as cells with significant stimulus-related fluorescence changes (ANOVA across blank and 12 direction periods, $P < 0.05$)[66].

The orientation and direction tuning curve was constructed by measuring the mean $\Delta F/F$, averaged over the stimulus period for each grating drifting direction θ, denoted as $R(\theta)$. The OSI was calculated for visually responsive units[21,66,67] with slight modifications on previous definitions[67] to avoid values outside the intended interval ([0 1]) and to accommodate occasional bona fide negative responses[68–70]. The preferred drifting direction (θ_{pref}) of the cell was determined as the stimuli that induced the greatest responses, $R(\theta_{pref})$ and $R(\theta_{oppo})$, as a sum where $\theta_{oppo} = \theta_{pref+180°}$, $R(\theta_{pref}) > R(\theta_{oppo})$. The OSI was defined as follows:

$$\text{OSI} = \frac{R(\theta_{pref}) + R(\theta_{oppo}) - R(\theta_{ortho+}) - R(\theta_{ortho-})}{R(\theta_{pref}) + R(\theta_{oppo})},$$

where $\theta_{orth+} = \theta_{pref+90°}$, $\theta_{orth-} = \theta_{pref-90°}$. All response values were subtracted by the most negative $R(\theta)$ when negative responses were present ($R_{corrected}$), which effectively ensured that the relative dynamic range of responses were reflected in the index for which they would otherwise distort the index (leading to values outside [0 1]), or be clipped (when negative values were discarded). Formally,

$$R_{corrected}(\theta) = R(\theta) - \min(0, R(\theta_{pref}), R(\theta_{oppo}), R(\theta_{orth+}), R(\theta_{orth-}))$$

Empirically, this modified index correlates tightly with the OSI calculated using the previous definition[67] of orientation index and OSI, is bounded by [0 1] and accommodates tuning curves that are partially or entirely negative. Notably, the trends and results of statistical comparisons in this work did not change with the choice of index definition. The DSI, global OSI (gOSI) and global DSI (gDSI) were defined as follows:

$$\text{DSI} = \frac{R(\theta_{pref}) - R(\theta_{oppo})}{R(\theta_{pref})}$$

$$\text{gOSI} = \frac{\left| \sum_k R(\theta_k) e^{i2\theta_k} \right|}{\sum_k R(\theta_k)}$$

$$\text{gDSI} = \frac{\left| \sum_k R(\theta_k) e^{i\theta_k} \right|}{\sum_k R(\theta_k)}$$

gOSI and gDSI gave the same conclusions as OSI and DSI (data not shown). Note that $R_{corrected}(\theta)$ can also be used in gOSI and gDSI, with the same benefits.

Head-fixed navigation and hippocampal imaging

Mice implanted with hippocampal imaging windows were subjected to a custom head-fixed virtual reality environment as previously described[41]. It consisted of a spherical treadmill monitored by an optical sensor that translated motion on the treadmill into forward motion through the virtual environment. We adjusted the forward gain so that 4 m of distance travelled along the circumference of the treadmill equalled one full traversal along a simulated linear track displayed on monitors surrounding the mouse. The track consisted of textured walls, floors and other 3D-rendered objects at the sides of the track as visual cues. To motivate consistent behaviour, we administered soy-milk rewards (4 µl) when the animal traversed certain locations that were spread at fixed distances along the track, and animals were trained for 5–10 days until they displayed consistent running behaviour before commencing imaging experiments.

Imaging was performed using a resonant/galvo high-speed laser scanning 2P microscope (Neurolabware) with a frame rate of 30 Hz for bidirectional scanning and a power of 5–20 mW measured at the objective front aperture. The microscope had an electrically tunable, fast z-focusing lens (Optotune, Edmund optics) to switch between z planes within less than a millisecond. Images were acquired through a ×16 objective (Nikon, 0.8 N.A., 3 mm WD). eGFP and jRGECO1a were excited at 930 nm or 1,040 nm, respectively, with a femtosecond-pulsed 2P laser (Mai Tai DeepSee, Spectra-Physics). We scanned 3 imaging planes (about 25 µm z spacing between planes) in rapid alternation so that each plane was sampled at 10 Hz. The planes spanned 300–500 µm in the x/y direction and were placed so that as many labelled neurons as possible were captured. We attached the animal's head plate to the bottom of an opaque imaging chamber before each experiment to block ambient light from the photodetectors. We fixed the chamber in the behavioural apparatus with the animal. A ring of black foam rubber between the imaging chamber and the microscope objective blocked any remaining stray light.

Spatial tuning analysis

We motion-corrected all imaging data line-by-line[71] with a 2D hidden Markov model using the software package SIMA[71] or with block-wise non-rigid registration through the software package Suite2P[72]. If no suitable motion correction could be achieved, we discarded the data. To segment interneuron somata, regions of interest (ROIs) were manually drawn using ImageJ (NIH) or automatically drawn by applying Suite2P[72]. For automated ROI settings, the experimenter subsequently inspected individual ROIs. The average jRGECO1a signal over time was then obtained from each ROI for all runs. We restricted our analysis to mouse running periods with a minimum speed of 5 cm s^{-1}. To obtain baseline-normalized $\Delta F/F$ calcium traces, we examined the fluorescence value distribution of the jRGECO1a signal and subtracted and divided the entire trace by the eighth percentile value of this distribution[73]. In rare instances, individual datapoints were below zero after baseline subtraction, and we set these negative values to zero for further calculations.

To compute spatial vector tuning, we plotted the mean activity ($\Delta F/F$) of each spatial bin at its respective angle from the start position on the

circular track into a polar coordinate system (Fig. 4e and Extended Data Fig. 15c). We then computed the circular mean of this distribution to obtain the mean tuning vector length and angle of the cell. Spatial coherence (Fig. 4f) was determined as the correlation (Pearson's R) between the mean fluorescence value in each 5-cm bin on the track and its two nearest neighbours, measuring the local smoothness of the spatial tuning curve[74]. To calculate spatial information (SI; Extended Data Fig. 15e), we computed the average calcium activity (mean $\Delta F/F$) for each 5-cm-wide bin along the linear track to approximate the average firing rate of neurons in that location. SI was then calculated for each cell as $SI = (\sum_{i=1}^{N} \lambda_i \log_2 \frac{\lambda_i}{\lambda} p_i) / \lambda$, where λ_i and p_i are the average calcium activity and fraction of time spent in the ith bin, respectively, λ is the overall calcium activity averaged over the entire linear track, and N is the number of bins on the track. Given the distribution of the underlying values, we plotted the $\log_{10}$ of SI values and compared them statistically (Extended Data Fig. 15e).

To assess the stability of the spatial representation of a cell within a session, we divided the track into 5-cm bins and calculated the mean $\Delta F/F$ value for each bin while the animal was moving on the track with a speed >5 cm s^{-1} to obtain activity maps for each individual cell. This mapping was done separately for the first and second half of the recording session. We then computed the within-session stability as the cross-correlation between the mean activity maps of the first and second half of the session (Extended Data Fig. 15b,f). We also computed population vector correlations as a function of position in the first and second half of the recording (Extended Data Fig. 15g) to visualize the local similarity of population activity across time. Before computing these correlations, we re-normalized the map of each neuron by subtracting the mean over space and dividing by the standard deviation (z scoring) to mitigate the potential effects of mean rate differences between cells on assessing local population vector similarity.

Quantification of *Gria2* mRNA A-to-I editing rates

We mapped the raw sequencing reads from a mouse brain scRNA-seq dataset ($n = 1,679$)[14] to the mouse reference genome (GRCm38) with a gene annotation, GENCODE (v.M16)[75], using STAR[76]. The uniquely mapped reads whose sequencing qualities (Phred score) were greater than 20 were counted for the QR and RG RNA-editing sites in *Gria2*. We filtered out samples if the proportions of the sequencing read with A or G alleles together accounted for less than 95% to avoid potential sequencing errors. We defined the RNA-editing rate for a given site as a ratio of the number of sequencing reads showing G relative to the number of reads with either A or G.

FACS-assisted RNA-seq of PV interneurons

To assess transcriptional changes specifically in PV interneurons after removing CP-AMPARs with RNA-seq, we sorted dissociated cortical PV interneurons by their GFP fluorescence using FACS. Dissociation of adult mouse brain neurons leads to a rapid decimation of viable PV interneurons[77-79], which potentially biases downstream analyses to a select subpopulation of PV interneurons. Various proposed methods to mitigate PV interneuron loss failed to recover them at native cell frequencies in adult mice[80]. Several fixation-based FACS approaches have been proposed to target immune cells and neurons, but crosslinking leads to lower RNA yield for RNA-seq.

We developed and used a brain-slice optimized workflow, FICSR-seq (Extended Data Fig. 11a), which recovers PV interneurons vulnerable to dissociation at native cell frequencies. We cut brain slices from adult mice (113.1 ± 11.6 days old) in NMDG cutting solution + trehalose[77] and diced them into small pieces <1 mm^3. Extracellular proteins were digested with pronase (2 mg ml^{-1}; 8 U µl^{-1}) at 34–37 °C, after which the slice pieces were fixed in 4% paraformaldehyde (PFA) in PBS (with 0.1 U ml^{-1} RNase inhibitor, Promega) for 15 min and dissociated into single cells through careful trituration. We filtered the single cells through a 40-µm filter, labelled them with the cell-permeable nuclear

dye DRAQ5 (1:1,000 dilution) to identify nuclei-containing cells and then subjected them to FACS. DRAQ5$^+$GFP$^+$ or DRAQ5$^+$GFP$^-$ cells were sorted, and more than 20,000 cells were collected per mouse cortex to provide extensive coverage of low-expressing PV interneuron transcripts.

We treated the fixed cells with proteinase K before RNA extraction (RecoverAll Total Nucleic Acid Isolation kit for FFPE, Thermo Fisher Scientific) to liberate RNA from protein–protein and protein–nucleic acid crosslinks generated by fixation. We prepared cDNA libraries from GFP$^+$ and GFP$^-$ samples (NEBNext Ultra RNA Library Prep kit for Illumina, NEB) from RNA enriched with mRNA through bead-based polyA selection. cDNA libraries were barcoded and sequenced together on an Illumina Hiseq 2500 sequencer, generating 150-bp paired-end reads. We processed RNA-seq reads with bcbio-nextgen (v.1.2.3; https://doi.org/10.5281/zenodo.3564938)[81], aligning to GRCm38 with the STAR aligner[76] and quantifying counts per gene with Sailfish[82] using the Ensembl annotation. We used DESeq2 (ref. 83) to analyse differential expression.

Brain slice preparation and whole-cell patch-clamp recordings

To test post-critical period electrophysiological properties and to maintain consistency within experiments, we used mice of either sex, aged postnatal day 32 (P32)–P62 for studies of synaptic properties and aged P69–P77 for studies of intrinsic properties. We first anaesthetized mice of either sex using isoflurane. We rapidly removed their brains in an ice-cold sucrose solution containing the following (in mM): 76 NaCl, 25 NaHCO$_3$, 25 glucose, 75 sucrose, 2.5 KCl, 1.25 NaH$_2$PO$_4$, 0.5 CaCl$_2$ and 7 MgSO$_4$, pH 7.3, 315 mOsm. We hemisected the brain along the midline and mounted one or both hemispheres on a 30° ramp. We then sectioned acute parasagittal slices of the visual cortex, 300-µm thick, in the same ice-cold sucrose-cutting solution using a vibratome (VT-1200s, Leica). Slices were incubated in warm (32–35 °C) sucrose solution for 30 min and then transferred to warm (32–35 °C) artificial cerebrospinal fluid (aCSF) composed of the following (in mM): 125 NaCl, 26 NaHCO$_3$, 2.5 KCl, 1.25 NaH$_2$PO$_4$, 1 MgSO$_4$, 20 D-(+)-glucose, 2 CaCl$_2$, 0.4 ascorbic acid, 2 pyruvic acid and 4 L-lactic acid, pH 7.3, 315 mOsm. Slices were then allowed to cool to room temperature. For rectification measurements, we cut coronal slices with a NMDG-based cutting solution and incubated them for >15 min. Then we transferred them to aCSF (see the section 'Analysis of AMPAR rectification'). All solutions were continuously equilibrated with 95% O$_2$ and 5% CO$_2$.

We transferred slices to a submersion chamber on an upright microscope (Zeiss AxioExaminer; ×40 objective, 1.0 NA) and continuously superfused (2–4 ml min^{-1}) them with warm (about 32–34 °C) oxygenated aCSF. We visualized neurons with a CCD camera (Sensicam QE, Cooke) using either infrared differential interference contrast (IR-DIC) microscopy or epifluorescence. The visual cortex was identified based on the relative position of the cortex and hippocampus and the anatomical borderline between the visual cortex and retrosplenial dysgranular cortex. We selected slices in which the apical dendrites of infragranular pyramidal neurons ran parallel to the plane of the slice up through L2/3 in the area targeted for recording. PV interneurons were targeted for recording based on eGFP or SEP-GluA2 expression along with unlabelled L2/3 pyramidal neurons. We filled patch pipettes (2–4 MΩ) pulled (P-97, Sutter Instrument) from borosilicate capillary glass (Sutter Instrument) with an internal solution containing (in mM): 2.7 KCl, 120 KMeSO$_3$, 9 HEPES, 0.18 EGTA, 4 ATP magnesium salt, 0.3 GTP sodium salt and 20 phosphocreatine disodium salt, adjusted to pH 7.3, 295 mOsm. For recordings of PV interneurons, the internal solution included 0.25% w/v biocytin. Whole-cell patch-clamp recordings were obtained using Multiclamp 700B amplifiers (Molecular Devices) and digitized using an Instrutech ITC-18 (HEKA) and software written in Igor Pro (Wavemetrics). All signals were low-pass filtered at 10 kHz and sampled at 20–100 kHz. Neurons with an access resistance >30 MΩ or a resting membrane potential greater than −60 mV were not used

for further recordings or analyses. The access resistance was not compensated in current clamp, and recordings were not corrected for the liquid junction potential.

Analysis of intrinsic excitability, synaptic connectivity and synaptic plasticity

We measured the resting membrane potential (RMP) shortly after establishing the whole-cell current-clamp recording configuration. A 1-s hyperpolarizing current (−100 pA) pulse was used to calculate the input resistance of recorded neurons. To assess the spiking behaviour of the cell, we injected 1-s depolarizing current steps into the recorded neurons. We measured the current–spike frequency relationship with a range of depolarizing current steps presented in pseudorandom order (1-s long, 40-pA increments, 5-s inter-stimulus intervals). Each current intensity was tested three times. For each current intensity, we counted the total number of action potentials exceeding an amplitude of 0 mV generated during each current step, then averaged the values across the three trials. We determined the rheobase by first probing the response of the neuron with 1-s-long depolarizing steps (5-s inter-stimulus intervals) to define a small range of current steps that bounded the rheobase. We then tested the neuron response within this range using 1-s-long depolarizing steps with 1-pA increments. We measured action potential properties from single spikes evoked by rheobase current injections. To compare the current–spike frequency relationship and rheobase between cells from the same baseline, we held cell membrane potentials at −70 mV when injecting depolarizing current steps. We performed all electrophysiological recordings that were assessing the intrinsic properties of PV interneurons in the presence of the following blockers of glutamate and GABA receptors (all from Tocris Bioscience): 5 µM NBQX (AMPA receptor antagonist); 5 µM (RS)-3-(2-carboxypiperazin-4-yl)-propyl-1-phosphonic acid (NMDA receptor antagonist); and 10 µM 6-imino-3-(4-methoxyphenyl)-1(6H)-pyridazinebutanoic acid hydrobromide (SR95531; GABA$_A$ receptor antagonist).

To determine the properties of unitary synaptic connections among neurons, we generated two action potentials in the presynaptic neuron by injecting short, depolarizing current steps (3-ms pulse duration, 20 Hz, 10-s inter-trial interval). We held pyramidal neurons and PV interneurons at approximately −55 mV and −70 mV during synaptic connectivity tests to detect inhibitory postsynaptic potentials (IPSPs) and EPSPs, respectively. We assessed synaptic connectivity (EPSP or IPSP) with an average of 10–50 trials. A synaptic connection was detected if the first response amplitude of the average trace was >3 times the root mean squared of the average trace during baseline conditions and visually verified. We calculated the paired-pulse ratio by dividing the amplitude of the second postsynaptic potential by the first.

We subjected a subset of connected pyramidal→PV pairs, all of which exhibited an average EPSP amplitude of >0.3 mV at baseline, to an anti-Hebbian protocol. After recording 50 traces (6 Hz) as a baseline, we induced synaptic plasticity by pairing 400 presynaptic action potentials delivered at 5 Hz with continuous hyperpolarization of the postsynaptic PV interneuron to −90 mV[25,84]. After induction, EPSPs were recorded under the same conditions as the baseline measurement (50 traces in response to presynaptic action potentials, 6 Hz).

Analysis of AMPAR rectification

To measure AMPAR rectification[85–88], we cut coronal brain slices in ice-cold cutting solution containing (in mM) 96 NMDG, 2.5 KCl, 1.25 NaH$_2$PO$_4$, 25 NaHCO$_3$, 25 D-(+)-glucose, 10 MgSO$_4$, 0.5 CaCl$_2$, 96 HCl, 20 HEPES, 12 N-acetylcysteine and 5 sodium L-ascorbate, and oxygenated with carbogen gas (95% O$_2$ and 5% CO$_2$). The 300-µm-thick slices were kept in aCSF (125 NaCl, 2.5 KCl, 2 MgCl$_2$, 2 CaCl$_2$, 1.0 NaH$_2$PO$_4$, 26.2 NaHCO$_3$ and 11 glucose) and oxygenated with carbogen gas at 23–25 °C until they were transferred for recording to a submerged chamber superfused with aCSF (1–3 ml min^{-1}) supplemented with about 50 µM

picrotoxin and 100 µM APV (2-amino-5-phosphonovaleric acid) to isolate AMPAR-mediated excitatory synaptic transmission.

We made targeted whole-cell recordings of eGFP/SEP-GluA2-positive L2/3 PV interneurons using pipettes of 3–5 MΩ resistance. The intracellular solution contained (in mM): 115 CsMeSO$_4$, 0.4 EGTA, 5.0 TEA-Cl, 1 QX314, 2.8 NaCl, 20 HEPES, 3.0 ATP magnesium salt, 0.5 GTP sodium salt, 10 phosphocreatine disodium salt and 0.1 spermine and was adjusted to pH 7.2, 285–290 mOsm. When we achieved whole-cell mode, we allowed >5 min for dialysis of the intracellular solution before collecting data. We held cells at −70 mV holding potential and recorded them at room temperature. We left the junction potential (about 11 mV) uncorrected. Signals were measured with a MultiClamp 700B amplifier, digitized using a Digidata 1440A digitizer (Molecular Devices) at 20 kHz and acquired with pClamp 10 software (Molecular Devices). We recorded AMPAR currents at 11 membrane potentials to construct a current–voltage (I–V) plot (V$_h$ = −60 to +60 mV, except for a subset of pyramidal neurons recorded for comparison up to +50 mV). We calculated the rectification index as a weighted ratio of negative (−60 mV) and positive (+60 mV) currents. We compensated for the junction potential (11 mV): rectification index (RI) = $(I_{-60 mV}/-71)/(I_{+60 mV}/49)$. An AMPAR rectification index of 1 represented perfect linearity, whereas values <1 indicate inward rectification. We estimated the reversal potential (E$_{rev}$) by cubic polynomial regression that fitted the linear, rectifying and double-rectifying AMPAR I–V curves well.

Immunohistochemistry

We deeply anaesthetized mice with isoflurane then transcardially perfused them with PBS and 4% PFA. We removed and post-fixed the brain in 4% PFA–PBS for >2 h. We sectioned the brain coronally into 25 µm slices using a vibratome (VT-1000, Leica). We acquired marmoset brains post-mortem from terminal experiments and sliced them into 40 µm sections. Free-floating sections underwent antigen retrieval using LAB solution (Polysciences) when necessary and were blocked and permeabilized in 3% BSA with 0.3% Triton X-100 in PBS for 1 h at room temperature. We incubated sections with primary antibodies overnight at 4 °C, washed them with PBS 3 times for 5 min, and then incubated them with secondary antibodies for 2 h at room temperature. After another round of washes, we mounted the slices on glass slides in PermaFluor mounting medium (Thermo Fisher Scientific) and imaged them using a laser scanning confocal microscope (Zeiss LSM880). Controls were carefully carried out, including antibody staining of homozygous knockout mice (Extended Data Fig. 2) to ensure antibody specificity. For GluA1 and GluA2 quantification, ROIs were made around cell somas, and the background signal was subtracted to estimate protein levels.

The following primary antibodies were used: rabbit anti-parvalbumin (1:2,000, PV25, Swant); goat anti-parvalbumin (1:1,000, PVG-213, Swant); rat anti-somatostatin (1:200, MAB354, Chemicon); mouse anti-CaMKIIα (1:1,000, sc-32288, Santa Cruz); rabbit anti-GluA1 (1:1,000, JH4294, generated in-house); mouse anti-GluA2 (1:5,000; clone 15F1, gift from E. Gouaux); chicken anti-GFP (1:1,000, GFP-1020, Aves); and rabbit anti-dsRed2 (1:1,000, 632496, Clontech). The following secondary antibodies were used: Alexa Fluor 405 donkey anti-goat (1:1,000, ab175665, Abcam); Dylight 405 goat anti-mouse IgG2a (1:1,000, 115-477-186 Jackson ImmunoResearch); Alexa Fluor 488 goat anti-mouse IgG2a (1:1,000, A-21131, Thermo Fisher Scientific); Alexa Fluor 488 goat anti-chicken (1:1,000, A-11039, Thermo Fisher Scientific); Alexa Fluor 546 goat anti-rabbit (1:1,000, A-11035, Thermo Fisher Scientific); Alexa Fluor 568 goat anti-mouse IgG1 (1:1,000, A-21124, Thermo Fisher Scientific); Alexa Fluor 568 goat anti-rabbit (1:500, Thermo Fisher Scientific); Texas Red donkey anti-goat (1:1,000, SAB3700332, Millipore Sigma); Alexa Fluor 647 goat anti-rabbit (1:1,000, A-21245, Thermo Fisher Scientific); Alexa Fluor 647 goat anti-mouse IgG2a (1:1,000, A-21241, Thermo Fisher Scientific); Alexa Fluor 647 donkey anti-goat

Article

(1:1,000, A-21447, Thermo Fisher Scientific); and Alexa Fluor 647 goat anti-rat (1:500, A-21247, Thermo Fisher Scientific).

Computational modelling

The low feature selectivity of PV neurons[17–21,89] (but see refs. 22,90–92) and the enhancement in PV-Cre;lsl-eGFP-GluA2 mice could result from several mechanisms. We used computational models to identify which mechanisms are consistent with the observed link between CP-AMPARs and feature selectivity. We examined the impact of three observed electrophysiological circuit changes: (1) increased intrinsic excitability (Extended Data Fig. 10o); (2) the loss of inward-rectifying AMPARs (Extended Data Fig. 7e,f); and (3) enhanced LTD (Extended Data Fig. 10l). Each mechanism was incorporated into a variation of a common base model. This model comprises a single PV neuron receiving excitatory inputs from a set of presynaptic pyramidal neurons with predefined stimulus tuning (Fig. 5a). The output of the PV neuron is a firing rate that is computed as a weighted sum of the inputs. Negative inputs are rectified to ensure a positive firing rate. To endow the PV neuron with stimulus tuning, pyramidal–PV connectivity was modelled as bell-shaped around the preferred orientation of the PV neuron (Fig. 5b), which enabled these neurons to inherit their tuning from pyramidal cells (Fig. 5c). We adjusted the parameters of pyramidal selectivity and connectivity to match the observed PV (and pyramidal) selectivity in the data.

Modelling increased intrinsic excitability

PV interneurons without CP-AMPARs showed increased intrinsic excitability (Extended Data Fig. 10o). PV neuron activation typically requires the coincident activation of multiple excitatory synaptic inputs[93,94]. However, the reduced rheobase, and increased RMP and input resistance in PV-Cre;lsl-eGFP-GluA2 mice suggested some strong synapses may reach the activation threshold unilaterally, which may increase selectivity[95]. To test whether this alone could account for the increased stimulus selectivity of PV interneurons, we increased the excitability of the PV model neuron by introducing a positive baseline current to the PV cell, mirroring the empirical shift of the frequency–current (F–I) curve (Extended Data Fig. 16a,b). We discovered that increased excitability reduced stimulus selectivity, contradicting the experimental observation. The response of the PV neuron was increased for all stimuli, thereby reducing the relative magnitude of the preferred response when compared with non-preferred responses (Extended Data Fig. 16c). This held for any rise in intrinsic excitability, regardless of a potential reduction in unitary EPSP amplitude (Extended Data Fig. 10f) when implemented as synaptic scaling (Extended Data Fig. 16d). We also simulated a scenario whereby enhanced intrinsic excitability was adjusted such that it homeostatically maintained the mean rate of the neuron by compensating for a multiplicative decrease in EPSPs (Extended Data Fig. 16e). In this scenario, stimulus selectivity was also reduced (Extended Data Fig. 16f–h). In conclusion, nonselective mechanisms such as increased intrinsic excitability and synaptic downscaling are insufficient to increase stimulus selectivity in the model.

Modelling removal of inward-rectifying AMPAR current

CP-AMPARs are inward-rectifying, which means that their conductance decreases with increasing postsynaptic potential (Extended Data Fig. 7e,f). This implies that they could become less effective for coincident stimuli that induce a strong postsynaptic response. To model this effect, we introduced a dependence of synaptic weights on the postsynaptic potential of the PV interneuron. In this model, we used conductance instead of current-based synapses to allow for a better comparison with experimentally measured current–voltage relationships. We modelled each synaptic weight as the sum of two components (Fig. 5d). The first represents CP-AMPARs and weakens with increasing postsynaptic potential. The second symbolizes other calcium-impermeable AMPARs

unaffected by postsynaptic potential (Fig. 5d, dashed line), except due to changes in synaptic drive. We systematically varied the amount of CP-AMPARs relative to calcium-impermeable AMPARs and the membrane potential at which they inactivate (inactivation threshold). The intuition behind CP-AMPARs influencing stimulus selectivity is that they should remain open for weak (that is, non-preferred) stimuli but deactivate for strong (that is, preferred) stimuli. PV neurons fire at high frequencies, which makes this more relevant, and compartmentalized dendritic depolarizations could further exacerbate this effect. This would selectively enhance the response to non-preferred stimuli, thus reducing stimulus selectivity. Conversely, eliminating CP-AMPARs would enhance stimulus selectivity. Indeed, we observed that removing the CP-AMPAR component reduced the response to non-preferred stimuli without affecting preferred stimuli, thereby increasing stimulus selectivity (Fig. 5e,f and compare with Extended Data Fig. 9c and Fig. 2e). This effect was robust to variations in the relative abundance of the CP-AMPARs and their inactivation threshold (Fig. 5g).

A qualitatively similar outcome emerged from applying a previously measured empirical I–V curve from Gria2^{−/−} mice[96] to estimate inward rectification (Extended Data Figs. 16 and 7e,f). Systematically varying the proportion of CP-AMPARs in the PV neuron model revealed that orientation selectivity monotonically decreases as the proportion of CP-AMPARs increases (Extended Data Fig. 16f). Two previous papers have examined the potential impact of CP-AMPARs on postsynaptic activation from slightly different perspectives of EPSC kinetics and dendritic summation sublinearity[93,97], and both arrived at conclusions similar to ours. In conclusion, increased stimulus selectivity may be due to the removal of CP-AMPAR-mediated inward rectification.

Modelling increased LTD

Pyramidal–PV connections exhibited exaggerated LTD in PV-Cre;lsl-eGFP-GluA2 mice compared with control mice (Extended Data Fig. 10l). This could enhance selectivity by weakening synaptic inputs from pyramidal cells tuned to non-preferred stimuli. We modelled this scenario by introducing synaptic plasticity in the pyramidal–PV synapses. Synaptic weights changed according to a Bienenstock–Cooper–Munro (BCM) rule, which has been broadly studied as a model for the development of stimulus selectivity[98]. The BCM learning rule is an associative rule that changes synapses when the presynaptic (pyramidal) neuron and the postsynaptic (PV) neuron are simultaneously active. However, the direction of the change is determined by the postsynaptic firing rate. When PV activity is below a threshold, synaptic efficacy decreases. If PV activity surpasses the threshold, synaptic efficacy increases (Fig. 5h). Here we used a fixed instead of the typical activity-dependent threshold in the classical BCM model. This allowed us to test the effect of increased LTD by varying the threshold. Specifically, we increased the LTP–LTD threshold to model the exaggerated LTD in PV-Cre;lsl-eGFP-GluA2 mice (Fig. 5h and Extended Data Fig. 10l). This weakened synapses from pyramidal cells activated for stimuli that elicit only a weak response in the PV cell (Fig. 5i). The exaggerated LTD consequently reduced the PV response to non-preferred stimuli (Fig. 5j) while enhancing its response to preferred stimuli. The resulting boost in selectivity was observable across a wide range of LTD–LTP thresholds as long as the threshold was within the range of PV responses (Fig. 5k). We conclude that increased selectivity could arise from changes in synaptic plasticity if this plasticity, in a BCM-like manner, can generate both potentiation and depression, and if depression is exaggerated after the removal of CP-AMPARs.

Conclusions of modelling studies

These modelling studies demonstrate that the inward-rectifying nature of the CP-AMPAR ion channel and the exaggerated LTD observed in PV-Cre;lsl-eGFP-GluA2 mice can both effectively reduce responses to non-preferred stimuli, thereby accounting for the increases in

orientation selectivity. However, neither the rise in intrinsic excitability nor a potential general reduction in excitatory input in PV interneurons due to GluA2 expression can explain the increase in orientation selectivity. These modelling findings imply that acute rectification and cumulative plasticity triggered by resident CP-AMPARs may sufficiently account for their role in maintaining low selectivity. Determining the extent of contribution of these two mechanisms to sensory selectivity in vivo poses a challenging question, which will necessitate rigorous empirical investigation in the future.

Network modelling architecture

The model was a feed-forward rate network of n presynaptic pyramidal neurons and a single postsynaptic PV neuron. We first describe the base model and then its elaborations. The presynaptic pyramidal neurons were tuned to stimulus direction and orientation according to a mixture of von Mises distributions. Specifically, the response of the ith pyramidal cell to a moving grating with direction θ was given by the following:

$$r_i(\theta) \propto (1-\alpha) \cdot \exp(\kappa \cdot \cos(\theta - \theta_i) + \alpha \cdot \exp(\kappa \cdot \cos(\theta - \theta_i - 180))$$

The proportionality sign indicates a normalization between a minimum of 0 and a maximum of 1 across stimuli. Here θ_i is the preferred direction of the cell, κ determines its tuning width and α controls the strength of direction tuning ($\kappa = 2$ and $\alpha = 0.5$). The preferred directions of the pyramidal cells were equally spaced in the interval $[0, 2\pi]$. The tuning of the PV cell was determined by the pyramidal tuning and the pyramidal-to-PV connectivity. Without loss of generality, we defined the preferred orientation of the PV cell to be 0°. The connectivity from the ith pyramidal cell onto the PV cell was given by a single von Mises distribution:

$$w_i \propto \exp(\kappa \cdot \cos(-\theta_i)), \kappa = 3$$

Weights were normalized across presynaptic cells, such that the minimum and maximum weights were equal to 0 and 1, respectively. The connectivity and pyramidal response together defined the PV voltage and rate using the following equations:

$$\tau \frac{du}{dt} = -u(t) + \sum_{i=1}^{n} w_i r_i(\theta)$$

$$r(t) = \max(u(t), 0).$$

Here, $\tau = 10$ ms denotes the membrane time constant. To simulate the PV activity from these equations, we used forward Euler discretization with a time step $\Delta t = 1$ ms. We simulated a time $T = 100$ ms unless specified otherwise and confirmed that the system had reached its steady state. This steady-state activity was used to compute tuning curves.

Intrinsic excitability. We fitted the change in the empirical I–F curve by numerically finding the shift that minimized the squared difference between the PV-Cre;lsl-eGFP-GluA2 and the PV-Cre;lsl-eGFP mean values. This was done using the minimize_scalar method of SciPy[99] with the shift as the optimization parameter. In the model, we increased the intrinsic excitability by adding an untuned positive baseline input I_0:

$$\tau \frac{du}{dt} = -u(t) + \sum_{i=1}^{n} w_i r_i(\theta) + I_0.$$

We varied I_0 between 0 and 10. Note that firing rates, membrane potential, weights and currents are unitless in our model. This does not alter the results, because orientation tuning is assessed based on relative rates. Decreases in unitary EPSPs were modelled by downscaling the synaptic weights with a factor p:

$$\tau \frac{du}{dt} = -u(t) + p \cdot \sum_{i=1}^{n} w_i r_i(\theta) + I_0.$$

We downscaled the weights in two different ways. In Extended Data Fig. 16d, we used $p = 0.62$, reflecting the mean empirical reduction in EPSPs (Extended Data Fig. 10f). To investigate the effect of homeostatic increases in excitability, we used the minimize_scalar function to find the scaling that would keep the average PV rate constant given a specific increase in its excitability I_0.

Inward rectification. We modelled the inward-rectifying calcium currents by adding a voltage-dependent weight scaling $p(u)$ to the PV dynamics. We also introduced conductance-based synapses to allow for a better comparison with experimental data:

$$\tau \frac{du}{dt} = -u(t) + p(u) \cdot \sum_{i=1}^{n} w_i r_i(\theta) \cdot \frac{u_0 - u}{u_0}.$$

Here, $u_0 = 30$ is the reversal potential. In our simulations, the precise value of u_0 and the choice for conductance versus current-based synapses scale the postsynaptic responses without strongly affecting relative stimulus tuning in different conditions. The scale p smoothly increases for decreasing voltages:

$$p(u) = 1 + \frac{A}{2} \cdot [\tanh(-\beta(u - M)) + 1].$$

This is a decreasing sigmoid function between 1 and A, with a slope β and a midpoint M. The midpoint M describes the threshold potential at which the CP-AMPARs deactivate, and β how sensitive the inactivation is to the membrane potential. A quantifies the abundance of rectifying AMPARs relative to the number of non-rectifying AMPARs. We varied A between 0 and 3 and M between 0 and 5; we fixed β to 0.5. The removal of CP-AMPARs was modelled by fixing p to 1. We increased the width of the presynaptic tuning to $\kappa = 3.6$ to achieve approximately equal selectivity in the presence of rectification.

In addition to this idealized model of inward rectification, we also simulated a data-driven model. Our starting point were previously measured current–voltage relationships[96] (Extended Data Fig. 16i). These data were collected in excitatory cells of wild-type and $Gria2^{-/-}$ mice, which allowed for a direct comparison of calcium permeable (CP) and calcium-impermeable (CI) receptors. Specifically, we used these published measurements[96] to estimate the normalized conductance at each voltage as the ratio I/V (Extended Data Fig. 16j). We did this for both wild-type and GluA2 traces, and normalized each between 0 and 1. This resulted in scaling factors $p_{CP}(u)$ and $p_{CI}(u)$ that represent the strength of CP and CI receptors, respectively, in our model (Extended Data Fig. 16k). Their convex sum determined the total synaptic rectification:

$$p(u) = \lambda \cdot p_{CP}(u) + (1 - \lambda) \cdot p_{CI}(u).$$

We found that orientation selectivity slowly but monotonically decreased with increasing λ (Extended data Fig. 16l–n). In the data-driven model, neurons with a larger relative abundance of CP receptors therefore have a weaker orientation selectivity, consistent with the idealized model and with our experimental findings.

Plasticity. We modelled synaptic plasticity using a plasticity rule inspired by BCM theory[98]. According to BCM, the change in synaptic efficacy is given by:

$$\Delta w = \eta \cdot r_{pre} \cdot r_{post} \cdot (r_{post} - \theta_{BCM}).$$

Article

Here $\eta = 0.02$ is a small learning rate that controls the speed of learning but does not affect the outcome. r_{pre} and r_{post} are the presynaptic and postsynaptic rates, respectively, and θ_{BCM} is the threshold between LTD and LTP. In most applications of the BCM rule, this threshold is adaptive and depends on the recent PV activity. Here we fixed it to a single value per experiment to allow full control over the amount of LTD. Specifically, LTD was implemented by increasing the threshold from 8 to 10 Hz. We further varied the threshold between 6.5 and 11 Hz. As the empirical response distribution seems to be largely unaffected by CP-AMPAR removal, we added synaptic scaling[100] to keep the mean postsynaptic rate constant:

$$w \rightarrow w \cdot \frac{r^*}{\bar{r}}.$$

Here r^* is the target mean rate, which we fixed to the mean rate across stimuli before the onset of plasticity. The mean rate $\bar{r}$ was computed after every weight update by averaging across all stimuli. In the plasticity experiments, we first simulated $T = 100$ time steps without plasticity to allow the system to reach a steady state. At subsequent time steps, we computed Δw for each individual stimulus, and used the average Δw across stimuli to update the weights. This continued until the weights and rates converged to a new steady state.

Statistical analysis and reproducibility
We performed statistical tests in Matlab (Mathworks), Prism (Graph-Pad) or R. Data distributions were tested for normality using Shapiro–Wilk test. We used parametric tests if the data were normally distributed and nonparametric otherwise, as detailed in the text describing each comparison. For parametric tests, we used unpaired or paired t-tests and one-way or two-way ANOVA tests with Tukey's post hoc multiple comparison correction (all two-sided). For data that did not follow normal or log-normal distributions, we used the following statistical tests where appropriate: Mann–Whitney U-test (Wilcoxon rank-sum test), Kruskal–Wallis one-way ANOVA with Dunn's post hoc multiple comparison correction (all two-sided). For categorical data, we used Fisher's test or χ^2 with or without Yates correction according to degrees of freedom and sample size. We report centre and spread values as the mean ± s.e.m. or median ± interquartile range unless otherwise stated. We did not use statistical methods to plan sample sizes, but used sample sizes similar to those frequently used in the field. The text or figure legends include the number of animals and cells. We did not use randomization, and data collection and analyses were not performed blind to the conditions of the experiments unless otherwise stated. P values < 0.05 were considered to be significant. When we used a statistical test, the P value is noted either in the manuscript text or depicted in figures and legends as follows: $*P < 0.05$, $**P < 0.01$, $***P < 0.001$, $****P < 0.0001$, NS, not significant, $P \geq 0.05$. Representative examples such as traces and micrographs were chosen from at least three or more independent experiments.

Reporting summary
Further information on research design is available in the Nature Portfolio Reporting Summary linked to this article.

Data availability
The data supporting the findings in this work are presented in the main figures and source data. Sequencing data included in this manuscript can be accessed at NCBI's Gene Expression Omnibus (GEO) under accession GSE262872. Other data of this study are available from the corresponding authors upon reasonable request. We used the following previously published datasets: adult mouse cortical cell taxonomy by single-cell transcriptomics[14] (GEO accession GSE71585);

neuronal subtypes and diversity revealed by scRNA-seq the human brain[27] (dbGaP study accession phs000833.v3.p1); and innovations in primate interneuron repertoire[28] (GEO accession GSE151761).

Code availability
Computer codes used to acquire data and analyse results of the study are available at GitHub (https://github.com/ingiehong/retinotopy, https://github.com/ingiehong/StackGPS and https://github.com/JoramKeijser/pv_selectivity) and from the corresponding author upon request.

51. Sousa, V. H., Miyoshi, G., Hjerling-Leffler, J., Karayannis, T. & Fishell, G. Characterization of Nkx6-2-derived neocortical interneuron lineages. *Cereb. Cortex* **19**, i1–i10 (2009).
52. Zamanillo, D. et al. Importance of AMPA receptors for hippocampal synaptic plasticity but not for spatial learning. *Science* **284**, 1805–1811 (1999).
53. Madisen, L. et al. A robust and high-throughput Cre reporting and characterization system for the whole mouse brain. *Nat. Neurosci.* **13**, 133–140 (2010).
54. Sekine-Aizawa, Y. & Huganir, R. L. Imaging of receptor trafficking by using α-bungarotoxin-binding-site-tagged receptors. *Proc. Natl Acad. Sci. USA* **101**, 17114–17119 (2004).
55. Dana, H. et al. Sensitive red protein calcium indicators for imaging neural activity. *eLife* **5**, e12727 (2016).
56. Choi, J. H. et al. Optimization of AAV expression cassettes to improve packaging capacity and transgene expression in neurons. *Mol. Brain* **7**, 17 (2014).
57. Dong, J. Y., Fan, P. D. & Frizzell, R. A. Quantitative analysis of the packaging capacity of recombinant adeno-associated virus. *Hum. Gene Ther.* **7**, 2101–2112 (1996).
58. Hoess, R., Wierzbicki, A. & Abremski, K. Formation of small circular DNA molecules via an in vitro site-specific recombination system. *Gene* **40**, 325–329 (1985).
59. Araki, Y., Lin, D. T. & Huganir, R. L. Plasma membrane insertion of the AMPA receptor GluA2 subunit is regulated by NSF binding and Q/R editing of the ion pore. *Proc. Natl Acad. Sci. USA* **107**, 11080–11085 (2010).
60. Wekselblatt, J. B., Flister, E. D., Piscopo, D. M. & Niell, C. M. Large-scale imaging of cortical dynamics during sensory perception and behavior. *J. Neurophysiol.* **115**, 2852–2866 (2016).
61. Juavinett, A. L., Nauhaus, I., Garrett, M. E., Zhuang, J. & Callaway, E. M. Automated identification of mouse visual areas with intrinsic signal imaging. *Nat. Protoc.* **12**, 32–43 (2017).
62. Pnevmatikakis, E. A. & Giovannucci, A. NoRMCorre: an online algorithm for piecewise rigid motion correction of calcium imaging data. *J. Neurosci. Methods* **291**, 83–94 (2017).
63. Giovannucci, A. et al. CaImAn an open source tool for scalable calcium imaging data analysis. *eLife* **8**, e38173 (2019).
64. Kleiner, M. et al. What's new in psychtoolbox-3. *Perception* **36**, 1–16 (2007).
65. Muir, D. R. & Kampa, B. M. FocusStack and StimServer: a new open source MATLAB toolchain for visual stimulation and analysis of two-photon calcium neuronal imaging data. *Front. Neuroinform.* **8**, 85 (2014).
66. Chen, T. W. et al. Ultrasensitive fluorescent proteins for imaging neuronal activity. *Nature* **499**, 295–300 (2013).
67. Mazurek, M., Kager, M. & Van Hooser, S. D. Robust quantification of orientation selectivity and direction selectivity. *Front. Neural Circuits* **8**, 92 (2014).
68. De Valois, R. L., Yund, E. W. & Hepler, N. The orientation and direction selectivity of cells in macaque visual cortex. *Vision Res.* **22**, 531–544 (1982).
69. Li, Y., Van Hooser, S. D., Mazurek, M., White, L. E. & Fitzpatrick, D. Experience with moving visual stimuli drives the early development of cortical direction selectivity. *Nature* **456**, 952–956 (2008).
70. Sclar, G. & Freeman, R. D. Orientation selectivity in the cat's striate cortex is invariant with stimulus contrast. *Exp. Brain Res.* **46**, 457–461 (1982).
71. Kaifosh, P., Zaremba, J. D., Danielson, N. B. & Losonczy, A. SIMA: Python software for analysis of dynamic fluorescence imaging data. *Front. Neuroinform.* **8**, 80 (2014).
72. Pachitariu, M. et al. Suite2p: beyond 10,000 neurons with standard two-photon microscopy. Preprint at *BioRxiv* https://doi.org/10.1101/061507 (2016).
73. Sheffield, M. E. J., Adoff, M. D. & Dombeck, D. A. Increased prevalence of calcium transients across the dendritic arbor during place field formation. *Neuron* **96**, 490–504.e5 (2017).
74. Kubie, J. L., Muller, R. U. & Bostock, E. Spatial firing properties of hippocampal theta cells. *J. Neurosci.* **10**, 1110–1123 (1990).
75. Frankish, A. et al. GENCODE reference annotation for the human and mouse genomes. *Nucleic Acids Res.* **47**, D766–D773 (2019).
76. Dobin, A. et al. STAR: ultrafast universal RNA-seq aligner. *Bioinformatics* **29**, 15–21 (2013).
77. Tasic, B. et al. Shared and distinct transcriptomic cell types across neocortical areas. *Nature* **563**, 72–78 (2018).
78. Joseph, D. J. et al. Protocol for isolating young adult parvalbumin interneurons from the mouse brain for extraction of high-quality RNA. *STAR Protoc.* **2**, 100714 (2021).
79. Zeisel, A. et al. Brain structure. Cell types in the mouse cortex and hippocampus revealed by single-cell RNA-seq. *Science* **347**, 1138–1142 (2015).
80. Saxena, A. et al. Trehalose-enhanced isolation of neuronal sub-types from adult mouse brain. *Biotechniques* **52**, 381–385 (2012).
81. Chapman, B. et al. bcbio/bcbio-nextgen v.1.2.9. *Zenodo* https://doi.org/10.5281/zenodo.3564938 (2021).
82. Patro, R., Mount, S. M. & Kingsford, C. Sailfish enables alignment-free isoform quantification from RNA-seq reads using lightweight algorithms. *Nat. Biotechnol.* **32**, 462–464 (2014).
83. Love, M. I., Huber, W. & Anders, S. Moderated estimation of fold change and dispersion for RNA-seq data with DESeq2. *Genome Biol.* **15**, 550 (2014).

84. Le Roux, N., Cabezas, C., Bohm, U. L. & Poncer, J. C. Input-specific learning rules at excitatory synapses onto hippocampal parvalbumin-expressing interneurons. *J. Physiol.* **591**, 1809–1822 (2013).

85. Hong, I. et al. AMPA receptor exchange underlies transient memory destabilization on retrieval. *Proc. Natl Acad. Sci. USA* **110**, 8218–8223 (2013).

86. Clem, R. L. & Huganir, R. L. Calcium-permeable AMPA receptor dynamics mediate fear memory erasure. *Science* **330**, 1108–1112 (2010).

87. Sommer, B., Kohler, M., Sprengel, R. & Seeburg, P. H. RNA editing in brain controls a determinant of ion flow in glutamate-gated channels. *Cell* **67**, 11–19 (1991).

88. Isaac, J. T., Ashby, M. C. & McBain, C. J. The role of the GluR2 subunit in AMPA receptor function and synaptic plasticity. *Neuron* **54**, 859–871 (2007).

89. Li, L. Y. et al. Differential receptive field properties of parvalbumin and somatostatin inhibitory neurons in mouse auditory cortex. *Cereb. Cortex* **25**, 1782–1791 (2015).

90. Runyan, C. A. & Sur, M. Response selectivity is correlated to dendritic structure in parvalbumin-expressing inhibitory neurons in visual cortex. *J. Neurosci.* **33**, 11724–11733 (2013).

91. Najafi, F. et al. Excitatory and inhibitory subnetworks are equally selective during decision-making and emerge simultaneously during learning. *Neuron* **105**, 165–179.e8 (2020).

92. Moore, A. K. & Wehr, M. Parvalbumin-expressing inhibitory interneurons in auditory cortex are well-tuned for frequency. *J. Neurosci.* **33**, 13713–13723 (2013).

93. Geiger, J. R., Lubke, J., Roth, A., Frotscher, M. & Jonas, P. Submillisecond AMPA receptor-mediated signaling at a principal neuron–interneuron synapse. *Neuron* **18**, 1009–1023 (1997).

94. Galarreta, M. & Hestrin, S. Spike transmission and synchrony detection in networks of GABAergic interneurons. *Science* **292**, 2295–2299 (2001).

95. Goetz, L., Roth, A. & Hausser, M. Active dendrites enable strong but sparse inputs to determine orientation selectivity. *Proc. Natl Acad. Sci. USA* **118**, e2017339118 (2021).

96. Lu, W. et al. Subunit composition of synaptic AMPA receptors revealed by a single-cell genetic approach. *Neuron* **62**, 254–268 (2009).

97. Cornford, J. *Computational Aspects of Parvalbumin-Positive Interneuron Function.* PhD thesis, Univ. College London (2017).

98. Bienenstock, E. L., Cooper, L. N. & Munro, P. W. Theory for the development of neuron selectivity: orientation specificity and binocular interaction in visual cortex. *J. Neurosci.* **2**, 32–48 (1982).

99. Virtanen, P. et al. SciPy 1.0: fundamental algorithms for scientific computing in Python. *Nat. Methods* **17**, 261–272 (2020).

100. Turrigiano, G. G. The self-tuning neuron: synaptic scaling of excitatory synapses. *Cell* **135**, 422–435 (2008).

101. Rodriguez, C. I. et al. High-efficiency deleter mice show that FLPe is an alternative to Cre-loxP. *Nat. Genet.* **25**, 139–140 (2000).

102. Hollmann, M., Hartley, M. & Heinemann, S. Ca^{2+} permeability of KA-AMPA-gated glutamate receptor channels depends on subunit composition. *Science* **252**, 851–853 (1991).

103. Verdoorn, T. A., Burnashev, N., Monyer, H., Seeburg, P. H. & Sakmann, B. Structural determinants of ion flow through recombinant glutamate receptor channels. *Science* **252**, 1715–1718 (1991).

Author contributions Generation of 2P imaging data: I.H., T. Hainmueller and T.C. Generation of electrophysiology data: I.H. and J. Kim. Generation of RNA-seq data: I.H., D.W.K., R.C.J., N.L., T. Hwang and F.M.K. Generation and validation of mice: I.H., Z.Y., D.C. and A.A. Generation of marmoset data: I.H., S.H.P. and D.A.L. Computational modelling: J. Keijser, H.S. and I.H. Data analyses: I.H., J. Kim, T. Hainmueller, D.W.K., R.C.J., S.H.P., N.L., Z.Y., D.C., T. Hwang, A.A., T.C., F.M.K., S.A.M., X.D., D.A.L., S.B., D.E.B., M.B., S.P.B. and R.L.H. Data interpretation: I.H., J. Kim, T. Hainmueller, D.W.K., S.H.P., S.B., D.E.B., M.B., S.P.B. and R.L.H. Writing the manuscript: I.H., J. Kim, T. Hainmueller, J. Keijser, H.S., D.A.L., D.E.B., M.B., S.P.B. and R.L.H.